

## 10. FROM OXIDIZING TO REDUCING ALTERATION: MINERALOGICAL VARIATIONS IN PILLOW BASALTS FROM THE EAST FLANK, JUAN DE FUCA RIDGE<sup>1</sup>

Pietro Marescotti,<sup>2</sup> David A. Vanko,<sup>3</sup> and Roberto Cabella<sup>2</sup>

### ABSTRACT

With this study, we investigate the mineralogical variations associated with the low-temperature (<100°C) alteration of normal tholeiitic pillow basalts varying in age from 0.8 to 3.5 Ma. Their alteration intensity varies systematically and is related to several factors, including (1) the aging of the igneous crust, (2) the increase of temperatures from the younger to the older sites, measured at the sediment/basement interface, (3) the local and regional variations in lithology and primary porosity, and (4) the degree of pillow fracturing. Fractures represent the most important pathways that allow significant penetration of fluids into the rock and are virtually the only factor controlling the alteration of the glassy rim and the early stages of pillow alteration. Three different alteration stages have been recognized: alteration of glassy margin, oxidizing alteration through fluid circulation in fracture systems, and reducing alteration through diffusion.

All the observed mineralogical and chemical variations occurring during the early stages of alteration are interpreted as the result of the rock interaction with “normal,” alkaline, and oxidizing seawater, along preferential pathways represented by the concentric and radial crack systems. The chemical composition of the fluid progressively evolves while moving into the basalt, leading to a reducing alteration stage, which is initially responsible for the precipitation of Fe-rich saponite and minor sulfides and subsequently for the widespread formation of carbonates. At the same time, the system evolved from being “water dominated” to being “rock dominated.” No alteration effects in pillow basalts were observed that must have occurred at temperatures higher than those measured during Leg 168 at the basement/sediment interface (e.g., between 15° and 64°C).

### INTRODUCTION

Pillow basalts, varying in age from around 0.8 to 3.5 Ma, were recovered during Leg 168 from nine sites (Sites 1023–1029 and 1031–1032), drilled across the eastern flank of the Juan de Fuca Ridge (JdFR). These sites are located from about 20 km to roughly 100 km east of the ridge axis and were subdivided into three main transects named the Hydrothermal Transition (HT, Sites 1023–1025), Buried Basement (BB, Sites 1028–1031), and Rough Basement (RB, Sites 1026 and 1027) transects, as described in the Leg 168 *Initial Reports* (Davis, Fisher, Firth, et al., 1997; Fig. 1).

As a consequence of the flat-lying sedimentary cover that onlaps the eastern flank of the JdFR, the present-day basement temperatures at the top of the volcanic sequence systematically increase from west to east along the transects, from 15°–38°C (HT), to 40°–59°C (BB), to 61°–64°C (RB).

The pillow basalts recovered from the three transects represent an ideal opportunity to study the effects of the low-temperature interaction between basalts and fluids (“normal” and “evolved” seawater) in contact with, or circulating within, the upper section of oceanic igneous crust.

With this study we document the petrography, mineralogy, and mineral paragenesis associated with the low-temperature alteration processes (<100°C) occurring in <3.5-Ma pillow basalts; the recovered massive units (Sites 1025, 1027, and 1032) and massive diabase (Site 1027) are not discussed in this manuscript. We give particular emphasis to the characterization of the transition from the oxidizing alteration style, which is related to open seawater circulation, to the reducing alteration style, which occurred under more restricted circu-

lation (i.e., at lower water/rock ratios) and lower  $f_{O_2}$  (oxygen fugacity).

### METHODS

Over 60 samples of pillow basalts representative of all nine sites were prepared and analyzed for the mineralogic and petrographic studies by optical microscopy, electron microprobe, X-ray diffraction (XRD), X-ray fluorescence (XRF), loss on ignition (LOI), and quantitative ferrous iron analyses.

Identification of mineral species was achieved by means of optical examinations under microscope (transmitted and reflected light) and XRD analyses on concentrated powder, using a Philips PW3710 diffractometer at the University of Genova, Italy. Samples were run between 2.5° and 70°2 $\theta$ , with a generator potential of 30 kV, a generator current of 22 mA (using a  $CuK_{\alpha}$  radiation), a Ni filter, and a scan speed of 1°/min. For XRD of the clay-sized fraction, the material was scraped from surface coating, open fractures, veins, vesicles, and cavities using dental tools and, when necessary, concentrated by settling in a water column. In addition, the clay-sized samples were saturated with ethylene glycol for 12 hr and reanalyzed to help identify expandable clay minerals. The software used for XRD data reduction was Philips PC-APD Diffraction Software and MacDiff 3.0.6c. Some nonclay minerals were determined by single crystal or separated aggregates analyses using a DIFFLEX II diffractometer equipped with a Gandolfi Camera ( $CuK_{\alpha}$ , Ni filter, 35kV/25mA, scan time = 6 hr).

Routine electron microprobe analyses were carried out with a Philips SEM 515 equipped with an energy-dispersive spectrometer (EDAX PV9100) at the University of Genova, Italy, and an ARL-SEMQ (WDS) microprobe at the University of Modena, Italy. Characteristic X-rays were detected using wavelength-dispersive spectrometers. Microprobe operating conditions were 15-kV accelerating voltage, 2- to 15-nA beam current, and 1- to 10- $\mu$ m beam diameter (up to 25  $\mu$ m for the glass and the clay minerals). Counting times of 120 s were reduced up to 60 s for clay minerals to prevent damage.

<sup>1</sup>Fisher, A., Davis, E.E., and Escutia, C. (Eds.), 2000. *Proc. ODP, Sci. Results*, 168: College Station TX (Ocean Drilling Program).

<sup>2</sup>Dipartimento per lo Studio del Territorio e delle sue Risorse, Università di Genova, I-16132 Genova, Italy. marescot@dister.unige.it

<sup>3</sup>Department of Geology, Georgia State University, Atlanta GA 30303, USA.

Calibration was accomplished with a range of synthetic and natural standards.

The modal abundance of secondary phases was calculated by point counting (based on 500 cts per section) on about 100 thin sections used for shorebased and shipboard analyses. The results were further checked against comparison charts for visual percentage estimation.

Representative samples of the various lithologies were selected and prepared as fused beads for major oxide analysis by XRF on a Philips PW1400 with a Rh anode X-ray tube. The gabbro MRG-1 and the basalt AII-92-29-1 international reference standards were used to calibrate the XRF spectrometer before running any unknown samples.

On 30 samples representative of all nine sites, quantitative ferrous iron analyses were performed at the Udine University, Italy, by  $KMnO_4$  titration on bulk rock powders after a  $HF + H_2SO_4$  acid attack. The values represent the average of five separate analytical

steps; the precision and the accuracy of this technique were checked periodically against the gabbro MRG-1 and the basalt AII-92-29-1 international reference standards, and analytical errors were always around  $\pm 0.1$  wt%.

Shipboard analyses done aboard the *JOIDES Resolution* included standard petrographic study with quantitative point counting, mineral analyses by XRD, whole-rock analyses by XRF, and LOI (Davis, Fisher, Firth, et al., 1997). These have been used to complete and compare the shorebased data set.

### PRIMARY PETROGRAPHIC AND MINERALOGIC FEATURES OF PILLOW BASALTS

In this section we describe and summarize the primary mineralogic and petrographic features of the Leg 168 pillow basalts. For a more detailed description see the Leg 168 *Initial Reports* (Davis, Fisher, Firth, et al., 1997).

Pillow basalts were recovered at the basement-sediment interface at nearly all sites (Sites 1023–1029 and 1031–1032; Table 1). Shore-based whole-rock major element analyses, together with shipboard analyses aboard the *JOIDES Resolution* (Davis, Fisher, Firth, et al., 1997) and shorebased analyses of other components of the Leg 168 Scientific Party (M. Constantin, pers. comm., 1998), indicate that most of the igneous rocks are low-K tholeiites. Four distinct geochemical groups have been distinguished on the basis of Mg#:

1. primitive pillow basalts from Site 1023 and from the lower subunits at Sites 1027 and 1032 (Mg# = 66–63);
2. slightly more fractionated pillow basalts from the upper subunits of the pillow lava sequence at Sites 1027 and 1032 and the pillow basalts from Sites 1024, 1026, 1028, and 1031 (Mg# = 63–56);
3. fractionated ferrobasalts from Site 1029 (Mg# = 53–40); and
4. highly fractionated ferrobasalts from the upper pillow unit overlying the massive lava sequence at Site 1025 (Mg# = 50–45).

The pillow basalts consist of aphyric (<1% phenocrysts) to moderately phyric (2%–10% phenocrysts) plagioclase  $\pm$  olivine  $\pm$  pyroxene or olivine  $\pm$  plagioclase basalts and show a low degree of vesicularity (<2%), with vesicles having diameters generally <1 mm.

Pillows commonly exhibit a distinct concentric structure as a consequence of the fast cooling conditions, which progressively decreases toward the pillow interior. From margin to core, five main zones (Fig. 2) have been distinguished, in good agreement with the previous observations of other authors (e.g., Baragar et al., 1977; Scott and Hajash, 1976; Juteau et al., 1980; Natland, 1980; Davis, Mottl, Fisher, et al., 1992): (1) glassy zone, (2) variolitic zone, (3) subvariolitic zone, (4) spherulitic zone, and (5) holocrystalline pillow core. Very small concentric cracks commonly mark the transitions from Zones 1 to 4, whereas the transition from Zone 4 to 5 is always graded without any sharp boundary.

1. The glassy zone consists of pale yellow to very light brown isotropic glass with scattered olivine microlites, plagioclase

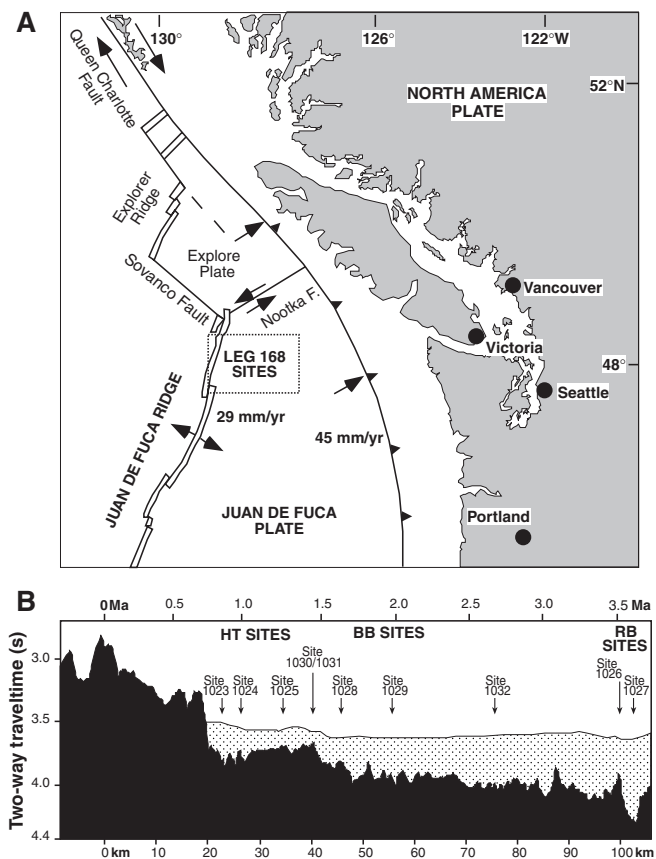


Figure 1. **A.** Location map of ODP Leg 168 (redrawn from Leg 168 Scientific Prospectus). **B.** Basement topography (black area) and sediment cover (stippled area), eastern flank of the Juan de Fuca Ridge (redrawn from Davis, Fisher, Firth, et al., 1997). HT = Hydrothermal Transition; BB = Buried Basement; RB = Rough Basement.

Table 1. Lithological summary of coring the Leg 168 sites.

Site	1023	1024	1025	1031	1028	1029	1032	1026	1027
Sediments cored (m)	193	168	98	41	133	220	290	229	569
Interbedded basalt talus, diabase, and hemipelagic mud cored (m)	None	None	None	None	None	None	None	None	37
Pillow basalt cored (m)	1	3	<1	1.5	1.1	2.9	48.1	66.3	26.2
Pillow basalt recovery	Trace	≤6%	Trace	35%	50%	52%	30%	4.5%	44.4%

Note: Data from Davis, Fisher, Firth, et al. (1997).

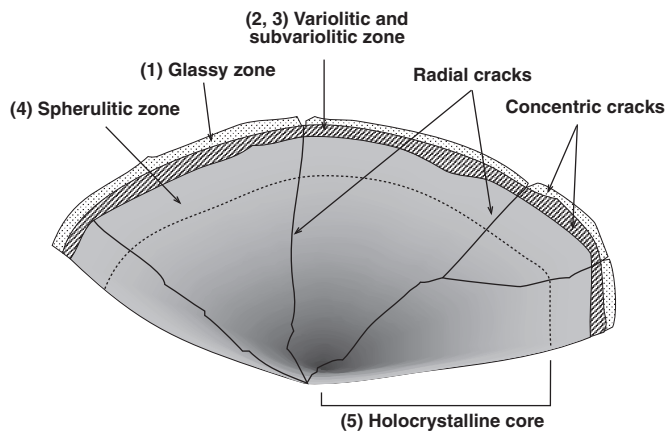


Figure 2. Location of structural zones and cracks in a pillow basalt. The thickness of the peripheral zones (up to 2 cm) are exaggerated for clarity; redrawn from Scott and Hajash (1976).

microlaths, and rare olivine  $\pm$  plagioclase phenocrysts (0.1–0.4 mm). The observed thickness in the recovered samples varies from <1 to 4 mm, but most of the glassy zones could have been broken up during the drilling operation. Nevertheless, only one section from Hole 1026B (Section 168-1026B-3R-1) consists of a strongly altered basalt-hyaloclastite breccia, containing angular clasts of aphyric basalt (with a variolitic to subvariolitic texture) and glassy shards, set within a consolidated clays  $\pm$  zeolites  $\pm$  carbonates matrix. The texture throughout the breccia varies from matrix supported to clast supported, and the dimension of the clasts generally is  $\leq$ 6 mm.

- The variolitic zone, 1–3 mm thick, consists of scattered ovoid brown varioles (0.03–0.08 mm in the longest dimension) isolated in the fresh isotropic glass. Varioles consist of a thin rim of fibrous anisotropic minerals (SEM analyses indicate that they probably correspond to intimate intergrowths of plagioclase and pyroxene fibers) centered on a plagioclase microclasts.
- The subvariolitic zone, 1–2 mm thick, is characterized by the progressive increase in the variole number and size from the outer margin towards the pillow interior. As the variole number increases, they progressively coalesce and the glass remains only in interstitial scattered areas.
- The spherulitic zone, 3–8 mm, is marked by the complete coalescence of the varioles that commonly form a dense polygonal net (honeycomb textures). The transition to the holocrystalline pillow interior (Zone 5) is marked by the progressive disappearance of varioles and by the development of different and various types of quench textures, such as plumose, branching, or sheaf spherulitic, indicating different nucleation and growth mechanisms mainly as a consequence of progressively slower cooling rates (McKenzie et al., 1982).
- In the pillow interior, the groundmass textures change from glomeroporphyritic, to intersertal, and finally to intergranular as the distance from the spherulitic zone increases. Simultaneously, the abundance of undifferentiated mesostasis areas decreases, and, when present, they occur in scattered, variably shaped, and irregularly distributed areas.

Euhedral plagioclase crystals (up to 1.5–1.7 mm in size) are the most abundant phenocryst species, often forming glomeroporphyritic aggregates; conversely, submillimetric euhedral to subhedral clinopyroxene and olivine phenocrysts (the latter completely replaced by secondary phases in almost all sites) commonly occur as isolated crystals or in biminerals associated with plagioclase.

The groundmass mainly consists of plagioclase laths and clinopyroxene micrograins with minor olivine, variable amounts of opaque oxides, and rare primary sulfides (pyrite, pyrrhotite, and chalcopyrite). Apatite whiskers commonly occur within or around plagioclase phenocrysts and laths.

## ALTERATION INTENSITY

Secondary alteration with variable intensity affects pillow basalts from all nine sites. Although local heterogeneities are common in every site, even at the scale of the individual sample, the alteration intensity systematically increases from the younger HT sites to the older RB sites. This general trend is clearly evidenced by alteration indexes such as the LOI value, the FeO/FeO<sub>i</sub> ratio, and the modal abundance of secondary minerals (Fig. 3).

The LOI (Fig. 3A) increases progressively from about 0.5 to 2 wt% with distance from the ridge axis, although local negative anomalies are evident in pillow basalts from Sites 1025 and subordinately 1029. Nevertheless, these anomalies are related to bulk rock composition, because the pillows from these sites are highly fractionated ferrobasalts and, consequently, the LOI value is strongly influenced by the oxidation of ferrous iron.

The FeO/FeO<sub>i</sub> value decreases progressively from 0.78 at Site 1023 to 0.61 at Site 1027 (Fig. 3B), mirroring the LOI pattern (Fig. 3A, B). In this context Site 1028 basalts show a very low FeO/FeO<sub>i</sub> value and a weak positive anomaly of LOI (Fig. 3A, B), suggesting a higher degree of alteration in comparison to the basalts of the other BB sites.

The total amount of alteration, determined by point counting the secondary minerals in thin section, varies from 0% at Site 1023 to 27% at Site 1027, with average values respectively varying from 0.2% to 12.73% (Fig. 3C). This distribution confirms the general increase of alteration with the distance from the ridge axis and the anomalous degree of alteration of pillow basalts from Site 1028.

Other alteration indicators such as the degree of vesicle fillings and the degree of olivine and glass alteration agree well with the indexes discussed above.

## SECONDARY MINERALS

The complete set of the recognized secondary phases together with their distribution and relative abundance in the pillow basalts from the different sites is reported in Figure 4. Secondary products are found mainly in four distinct modes of occurrence: (1) vesicle or cavity linings or fillings; (2) coatings, fracture fillings, and veins; (3) pseudomorphic replacement of mafic phenocrysts and microphenocrysts (mainly olivine and subordinately clinopyroxene); and (4) patches within mesostasis.

### Clay Minerals

Clay minerals are ubiquitous and are the most abundant secondary products, present in all four modes discussed above. Clay minerals were determined optically, following the criteria of Honnorez et al. (1983) and Laverne et al. (1996), by XRD data, including those of air-dried and glycolated powder mounts, and by microprobe quantitative and semiquantitative analyses.

XRD data of clay minerals indicate that trioctahedral smectite is the predominant phyllosilicate ( $d_{001} = 13\text{--}15 \text{ \AA}$  expanding after glycolation to  $d_{001} = 17.1\text{--}17.8 \text{ \AA}$  and  $d_{060} = 1.53 \text{ \AA}$ ; Fig. 5). Subordinate types of mixed-layer clays, or mechanical mixtures of two or more clays, have been recognized: celadonite-smectite (Sites 1024–1029 and 1031–1032), celadonite-smectite-nontronite (Sites 1026–1027, 1029, 1032), smectite-chlorite (Sites 1027 and 1032), and smectite-montmorillonite (Sites 1027 and 1032).

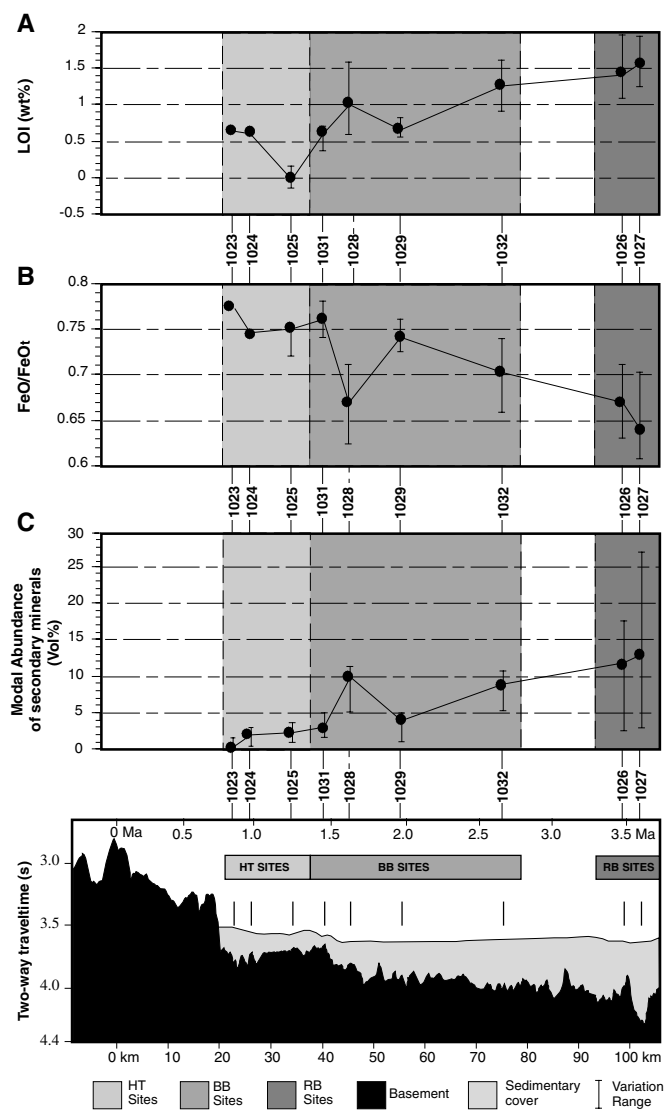


Figure 3. Variations of secondary alteration indexes with distance from the ridge axis. **A.** Loss on ignition (LOI wt%). **B.** FeO/FeO<sub>1</sub> value. **C.** Modal abundance of secondary minerals (vol%). Solid circles = medium values; bars = variation range.

Only one sample (Sample 168-1029A-25X-3, 77–82 cm) gave an X-ray spectrum unequivocally referable to a dioctahedral mica (celadonite type, Fig. 6), although there is evidence that trioctahedral smectite and possible smectite-celadonite mixed-layer minerals are present (as evidenced by the  $d_{060} = 1.532 \text{ \AA}$  reflection of smectite together with the  $d_{060} = 1.509 \text{ \AA}$  reflection of celadonite; Fig. 6).

On the basis of mineral chemistry and optical features we have distinguished five main different types of clay minerals or clay mixtures (as schematized in Table 2; Types 1–5), which can be classified into two main groups: saponite group and celadonite or celadonite mixtures group.

#### Saponite Group

Saponite is the most common clay, and it has been identified at all sites. On the basis of more than 140 microprobe analyses, two sub-groups may be divided (Types 1 and 2; Table 2): (1) Fe-rich saponites (MgO = 13–19 wt%; FeO<sub>1</sub> = 13–21 wt%); and (2) Mg-rich saponites (MgO = 18–23 wt%; FeO<sub>1</sub> = 8–12 wt%). Whereas Mg-rich saponite

occurs often associated with celadonite and subordinately to Fe-oxyhydroxides in fractures or adjoining oxidation halos, Fe-rich saponite is restricted to the reducing assemblages together with carbonates and sulfides. Both saponite types are present as vesicle fillings, patches within mesostasis, fracture coatings and vein fillings, and pseudomorphic replacement of mafic minerals (mainly olivine).

Analyses were calculated on the basis of 20 oxygens and four hydroxyls (Table 3). Structural formulas were calculated considering that  $(\text{Si} + \text{Al})^{\text{IV}} = 8$  atoms per formula unit (a.p.f.u.); the excess Al was assigned to octahedral sites together with Fe<sub>1</sub> and Mg. When present, the slight excess of Mg in octahedral sites was placed in interlayer positions as an exchange cation. The compositional variations of the two saponite types (Table 3) agree well with the chemical constraints suggested by Andrews (1980) and reveal a considerable range of Fe-Mg substitution in octahedral coordination (Fig. 7), with the higher Fe contents occurring in samples from Site 1025 (i.e., in the fractionated ferrobalt). Interlayer sites are mainly occupied by Ca and subordinately by K and Mg, whereas Na is generally below the detection limits.

#### Celadonite or Celadonite-Bearing Mixtures Group

Material identified as celadonite during Leg 168 shipboard analyses (Davis, Fisher, Firth, et al., 1997) appears in hand specimen as green to very dark green with resinous luster and waxy consistency, and in thin section as bright green to yellow-green cryptocrystalline or fibrous aggregates (Types 3–5; Table 2). Nevertheless (as discussed above), only one sample from Site 1029 shows an XRD pattern corresponding to a dioctahedral mica of the celadonite type. Celadonite or celadonite-bearing mixtures mainly occur within fractures and veins or in adjacent greenish and subordinately reddish brown halos (as vesicle fillings, irregular patches or pseudomorphic replacements).

Microprobe analyses were calculated on the basis of 20 oxygens and four hydroxyls per unit cell (Table 4). Aluminum was distributed between tetrahedral and octahedral coordination so that the tetrahedral occupancy  $(\text{Si} + \text{Al})$  always sums to 8 a.p.f.u. No normalizations were performed for the octahedral sites to verify the possible excess of occupancy. Following these assumptions, all celadonite analyses invariably exhibit a large excess of cations in octahedral coordination (from 4.70 to 5.43 a.p.f.u.) compared to a value of 4.00 a.p.f.u. required by the dioctahedral structure. As evidenced in Figure 8, the octahedral occupancy excess shows a significant positive correlation with the total Fe content (a.p.f.u.). This evidence suggests that the high octahedral total is mainly related to the presence of a finely intermixed Fe-oxide contaminant extraneous to the celadonite structure and/or to the presence of interlayered Fe-rich smectite (as discussed by Andrews [1980] and Li et al. [1997]). TEM observations, performed on celadonites by Peacor (1992) and Li et al., (1997) demonstrate that submicrometer mixed layering is a common feature in celadonites formed at low temperatures.

#### Fe-oxyhydroxides and Mixtures of Fe-oxyhydroxides and Clay Minerals

Fe-oxyhydroxides and mixtures of Fe-oxyhydroxides and clay minerals strictly occur within fractures and veins or in reddish brown halos immediately around them (as vesicle filling, irregular patches within mesostasis, or pseudomorphic replacements). They commonly occur alone or associated with celadonite or celadonite mixtures. Most of the Fe-rich compounds actually correspond to mixtures of Fe-oxyhydroxides and clay minerals (iddingsite), although optical examinations under microscope (reflected light) and microprobe analyses suggest the presence of pure and finely disseminated goethite and/or hematite lamellae in some microveins from Sites 1026 to 1027 and 1032.

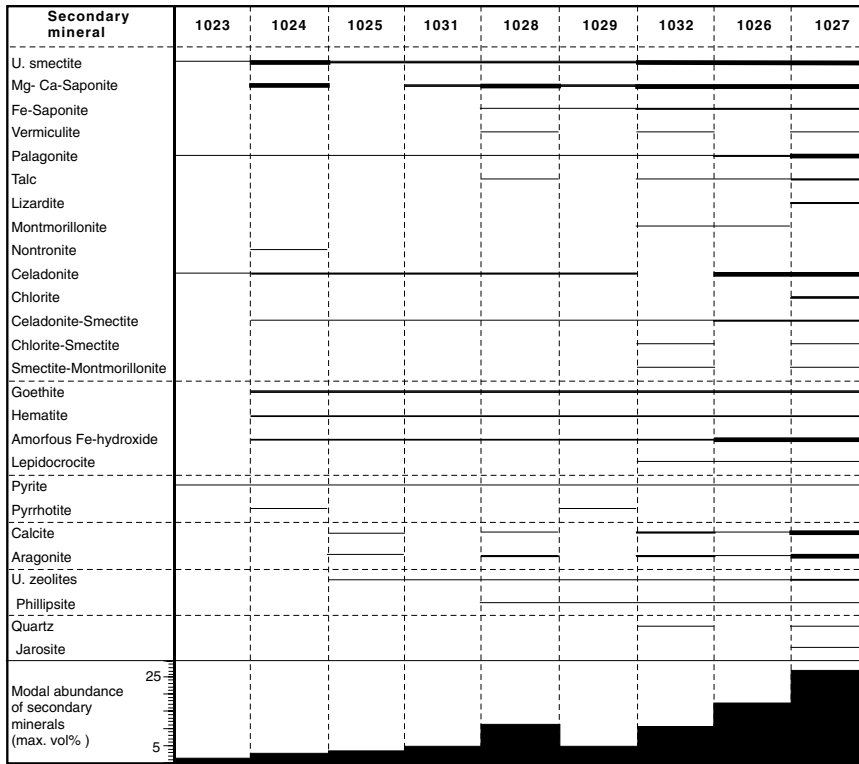


Figure 4. Distribution and relative abundance of secondary minerals in pillow basalts from Sites 1023 to 1032. U. smectite = undifferentiated trioctahedral smectite; U. zeolites = undifferentiated zeolites.

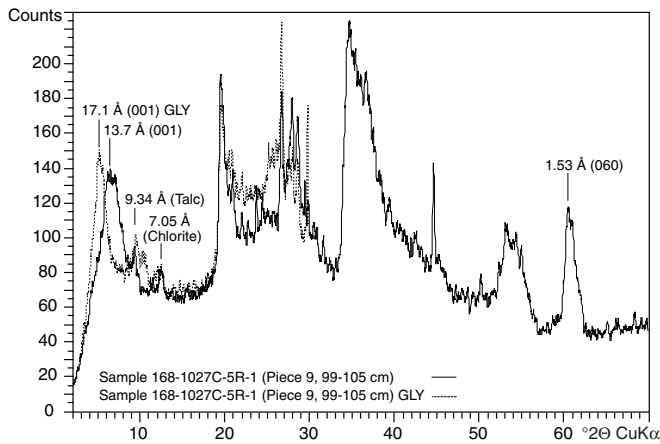


Figure 5. Multiple XRD patterns of trioctahedral smectite showing the  $d_{001}$  and  $d_{060}$  reflections. The  $d_{001}$  reflection shift from 13.7 to 17.1 Å after glycolation. The peaks at 9.34 Å and 7.05 Å, not expanding after glycolation, suggest the presence of talc and chlorite respectively. GLY = XRD pattern after glycolation.

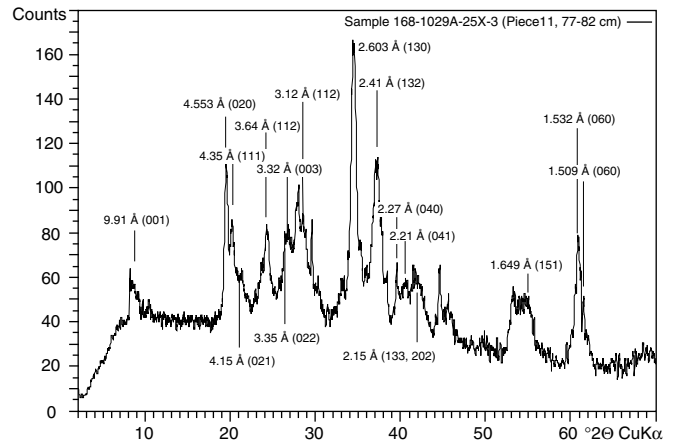


Figure 6. XRD pattern of dioctahedral mica (celadonite). Celadonite reflections have been indexed as in Wise and Eugster (1964) and Li et al. (1997). The  $d_{060}$  reflection = 1.532 Å suggests minor amount of trioctahedral smectite.

Mixtures have been divided into four main types (Types 6–9; Table 2) on the basis both of the optical features (mainly the color in plane-polarized light) and chemical composition. Types 6 and 7 mixtures appear in thin section as massive aggregates of cryptocrystalline material varying in color respectively from bright orange yellow to orange red. As evidenced in SEM microphotographs, they clearly represent heterogeneous mixtures of Fe-oxyhydroxides or iddingsitic material and celadonite with the celadonite content progressively decreasing from Type 6 to 7 (Pl. 1; Figs. 1, 2).

Types 8 and 9 correspond to iddingsitic mixtures that appear, both in hand specimen and thin section, as dense compounds varying in color respectively from dark brownish red to dark bright red. The

mixture between Fe-oxyhydroxides and undifferentiated clay minerals is never discernible even at the resolution limits of the SEM, and consequently the actual end member cannot be recognized. The chemical composition of the two types is comparable ( $FeO_t = 65\text{--}70$  wt%;  $SiO_2 = 9\text{--}12$  wt%; and minor amounts [always <1 wt%] of  $CaO$ ,  $K_2O$ , and  $MgO$ ), and no major variations correspond to the observed change in color.

### Carbonates

Calcite and aragonite are widely distributed in pillow basalts, massive basalts, and diabase, although these minerals are not ubiquitous. Calcium carbonate occurs alone or associated with saponite in

**Table 2. Main characteristics of clay minerals and clay mixtures.**

Type	Site	Shape	Pleochroism	Color with crossed polars	Mode of occurrence	Where	Associated minerals	Dominant chemical feature	Mineral	
1	Pale brown	1025, 1027, 1028, 1032	Fibers or cryptocrystalline granules	Nonexistent	Gray first order	M1-M4	GI	Carbonates, sulfides	High FeO <sub>t</sub> , low MgO	Fe-rich saponite
2	Very pale green	1023, 1024, 1026, 1027, 1028, 1029, 1031, 1032	Fibers or rare cryptocrystalline granules	Nonexistent	Gray first order to orange	M1-M4	TZ	Celadonite, Fe-rich saponite, iddingsite	High MgO, low FeO <sub>t</sub>	Mg-rich saponite
3	Bright green	1029	Cryptocrystalline massive aggregates	Slight	Second order often masked by the green color	M1, M3, M4	GH, RH, TZ	Iddingsite, Mg-rich saponite, Fe-oxyhydroxides	High K <sub>2</sub> O, medium FeO <sub>t</sub>	Celadonite
4	Green	1023, 1024, 1026, 1027, 1028, 1029, 1031, 1032	Fibers	Nonexistent	Masked by the color	M1-M4	GH, RH, TZ	Iddingsite, Mg-rich saponite, Fe-oxyhydroxides	Medium K <sub>2</sub> O, medium FeO <sub>t</sub>	Saponite-celadonite mixtures
5	Yellow green	1023, 1024, 1026, 1027, 1028, 1029, 1031, 1032	Fibers	Nonexistent	Masked by the color	M1-M4	GH, RH, TZ	Iddingsite, Mg-rich saponite, Fe-oxyhydroxides	Medium K <sub>2</sub> O, medium FeO <sub>t</sub>	Saponite-celadonite or saponite-nontronite mixtures
6	Bright orange yellow	1023, 1024, 1026, 1027, 1028, 1029, 1031, 1032	Fibers or cryptocrystalline granules	Nonexistent	Masked by the color	M1-M4	RH, GH	Iddingsite, Fe-oxyhydroxides	Medium K <sub>2</sub> O, medium FeO <sub>t</sub>	Iddingsite-celadonite mixtures
7	Orange to red	1023, 1024, 1026, 1027, 1028, 1029, 1031, 1032	Cryptocrystalline granules	Nonexistent	Masked by the color	M1-M4	RH, GH	Iddingsite, Fe-oxyhydroxides	Low K <sub>2</sub> O, high FeO <sub>t</sub>	Iddingsite-celadonite mixtures
8	Dark brownish red	1023, 1024, 1026, 1027, 1028, 1029, 1031, 1032	Massive cryptocrystalline aggregates	Nonexistent	Almost opaque	M1, M2	RH	Fe-oxyhydroxides, celadonite	Very high FeO <sub>t</sub> , medium SiO <sub>2</sub>	Iddingsite
9	Dark bright red	1023, 1024, 1026, 1027, 1028, 1029, 1031, 1032	Massive cryptocrystalline aggregates	Nonexistent	Almost opaque	M1, M2	RH	Fe-oxyhydroxides, celadonite	Very high FeO <sub>t</sub> , low SiO <sub>2</sub>	Iddingsite

Notes: M1= vesicle or cavity linings or fillings; M2 = fracture and veins coatings and fillings; M3 = pseudomorphic replacement; M4 = patches within mesostasis; GI = gray interior; TZ = transition zone between oxidation halos and gray interior; RH = red halos; GH = green halos. Made following the scheme of Laverne et al. (1996).

Table 3. Representative analyses of Mg-rich and Fe-rich saponites.

Core:	1024B	1025B	1026C	1026C	1026C	1026C	1027C	1028A	1028A	1028A	1028A	1028A	1029A	1029A	1031A	1031A	1031A	1031A	1032A	1032A																							
section:	18X-CC	11X-CC	16R-1	17R-1	17R-1	17R-1	5R-5	4R-3	4R-3	4R-3	5R-5	5R-5	3R-2	3R-2	15X-7	15X-7	15X-7	15X-7	25X-4	25X-3	6X-1	6X-1	6X-1	12R-1	12R-1																		
Interval (cm):	10-37	34-40	40-45	13-17	13-17	13-17	22-27	85-91	85-91	85-91	22-27	22-27	115-117	115-117	15-18	15-18	15-18	15-18	7-12	77-82	49-52	49-52	49-52	126-132	126-132																		
Piece:	1	2	20	4	4	4	2	10	10	10	2	2	-	-	2	2	2	2	2	11	10	10	10	19	19																		
Depth (mbsf):	167.83	97.53	238.90	238.63	238.63	238.63	628.95	617.49	617.49	617.49	628.95	628.95	606.25	606.25	132.89	132.89	132.89	132.89	221.14	220.57	41.79	41.79	41.79	291.46	291.46																		
Mineral	Fe-rich	Fe-rich	Mg-rich	Mg-rich	Mg-rich	Fe-rich	Mg-rich	Fe-rich	Mg-rich	Mg-rich	Mg-rich	Mg-rich	Mg-rich	Fe-rich	Mg-rich																												
SiO <sub>2</sub>	49.83	48.01	47.87	47.34	48.52	49.88	52.52	50.36	50.48	51.23	49.30	50.16	49.34	47.60	50.56	48.25	47.81	50.52	49.58	48.37	45.80	49.03	48.64	49.44	49.58																		
TiO <sub>2</sub>	0.04	0.43	0.02	0.04	0.01	0.12	0.04	0.00	0.07	0.00	0.05	0.04	0.06	0.00	0.00	0.00	0.01	0.00	0.00	0.00	0.04	0.09	0.20	0.00	0.04																		
Al <sub>2</sub> O <sub>3</sub>	3.22	2.96	3.48	3.79	3.99	3.73	2.68	3.22	3.26	3.42	3.84	3.84	4.89	4.15	2.89	3.86	3.98	3.87	3.18	4.70	4.28	4.18	4.49	3.52	3.69																		
Fe <sub>2</sub> O <sub>3</sub>	0.08	0.06	0.06	0.00	0.00	0.00	0.22	0.00	0.00	0.00	0.00	0.00	0.00	0.00	0.00	0.00	0.00	0.00	0.00	0.00	0.00	0.00	0.00	0.00	0.00																		
FeO	13.72	21.56	11.09	11.32	11.99	13.18	8.85	9.57	9.71	9.82	10.05	10.30	12.35	13.24	10.33	12.48	12.82	12.86	11.83	14.18	10.90	11.99	12.16	7.99	8.57																		
MgO	18.74	13.64	19.20	19.34	19.65	19.42	22.25	21.03	21.20	21.64	20.76	21.48	20.02	18.81	20.74	18.91	18.50	20.21	19.66	18.64	18.51	19.03	19.43	22.00	21.50																		
MnO	0.00	0.21	0.01	0.19	0.02	0.12	0.14	0.11	0.06	0.20	0.20	0.22	0.10	0.11	0.17	0.08	0.19	0.31	0.00	0.24	0.18	0.21	0.19	0.06	0.08																		
NiO	0.15	0.00	0.00	0.37	0.30	0.13	0.03	0.05	0.11	0.07	0.53	0.41	0.08	0.08	0.01	0.00	0.00	0.13	0.56	0.19	0.30	0.28	0.32	0.09	0.13																		
CaO	0.95	1.59	1.20	1.11	1.11	1.07	1.16	1.29	1.29	1.33	1.42	1.51	1.36	1.51	0.90	1.08	1.66	1.25	1.08	1.56	0.90	1.13	1.15	1.10	1.07																		
Na <sub>2</sub> O	0.00	0.00	0.00	0.00	0.00	0.00	0.00	0.00	0.00	0.00	0.00	0.00	0.00	0.11	0.00	0.00	0.00	0.00	0.00	0.00	0.00	0.00	0.00	0.00	0.00																		
K <sub>2</sub> O	0.40	0.27	0.09	0.22	0.08	0.11	0.27	0.12	0.13	0.13	0.22	0.14	0.22	0.11	0.43	0.51	0.00	0.51	0.57	0.16	0.44	0.31	0.39	0.32	0.26																		
Total	87.13	88.73	83.02	83.72	85.67	87.76	88.16	85.75	86.31	87.84	86.37	88.10	88.42	85.72	86.03	85.17	84.97	89.66	86.46	88.04	81.35	86.25	86.97	84.52	84.92																		
Si	7.493	7.418	7.457	7.359	7.366	7.418	7.591	7.519	7.496	7.479	7.375	7.356	7.269	7.293	7.558	7.397	7.360	7.371	7.474	7.248	7.324	7.399	7.302	7.446	7.448																		
Al <sup>(IV)</sup>	0.507	0.539	0.543	0.641	0.634	0.582	0.409	0.481	0.504	0.521	0.625	0.644	0.731	0.707	0.442	0.603	0.640	0.629	0.526	0.752	0.676	0.601	0.698	0.554	0.552																		
Ti	0.005	0.050	0.002	0.005	0.001	0.013	0.004	0.000	0.008	0.000	0.006	0.004	0.007	0.000	0.000	0.000	0.001	0.000	0.000	0.000	0.005	0.010	0.023	0.000	0.005																		
Al <sup>(VI)</sup>	0.064	0.000	0.095	0.054	0.079	0.072	0.047	0.085	0.067	0.067	0.052	0.019	0.118	0.042	0.067	0.095	0.082	0.036	0.038	0.078	0.131	0.142	0.096	0.070	0.102																		
Fe <sub>T</sub>	1.725	2.786	1.445	1.472	1.522	1.639	1.070	1.195	1.206	1.199	1.257	1.263	1.522	1.696	1.291	1.600	1.651	1.569	1.491	1.777	1.458	1.513	1.527	1.006	1.077																		
Cr	0.010	0.007	0.007	0.000	0.000	0.000	0.025	0.000	0.000	0.000	0.000	0.000	0.000	0.000	0.000	0.000	0.000	0.000	0.000	0.000	0.000	0.000	0.000	0.000	0.000																		
Mg <sup>(VI)</sup>	4.179	3.129	4.449	4.399	4.358	4.245	4.793	4.680	4.692	4.701	4.596	4.637	4.332	4.238	4.619	4.295	4.241	4.341	4.402	4.092	4.344	4.274	4.292	4.905	4.791																		
Mn	0.000	0.027	0.001	0.025	0.003	0.015	0.017	0.014	0.008	0.025	0.025	0.027	0.012	0.014	0.022	0.010	0.025	0.038	0.000	0.030	0.024	0.027	0.024	0.008	0.010																		
Ni	0.018	0.000	0.000	0.046	0.037	0.016	0.003	0.006	0.013	0.008	0.064	0.048	0.009	0.010	0.001	0.000	0.000	0.015	0.068	0.023	0.039	0.034	0.039	0.011	0.016																		
Mg	0.021	0.012	0.009	0.082	0.088	0.060	0.000	0.000	0.007	0.033	0.058	0.064	0.058	0.002	0.027	0.004	0.054	0.015	0.071	0.069	0.007	0.056	0.034	0.023	0.023																		
Ca	0.153	0.263	0.200	0.185	0.181	0.170	0.180	0.206	0.205	0.208	0.228	0.237	0.215	0.248	0.144	0.177	0.274	0.195	0.174	0.250	0.154	0.183	0.185	0.177	0.172																		
Na	0.000	0.000	0.000	0.000	0.000	0.000	0.000	0.000	0.000	0.000	0.000	0.000	0.000	0.033	0.000	0.000	0.000	0.000	0.000	0.000	0.000	0.000	0.000	0.000	0.000																		
K	0.077	0.053	0.018	0.044	0.015	0.021	0.050	0.023	0.025	0.024	0.042	0.026	0.041	0.021	0.082	0.100	0.000	0.095	0.110	0.031	0.090	0.060	0.075	0.061	0.050																		

Notes: Formulas have been calculated on the basis of 20 oxygens and four hydroxyls per unit cell, considering (Si + Al)<sup>IV</sup> = 8 a.p.f.u. and assigning the remaining Al to the octahedral sites together with Fe and Mg. The Mg excess in octahedral sites has been assigned to the interlayer positions.

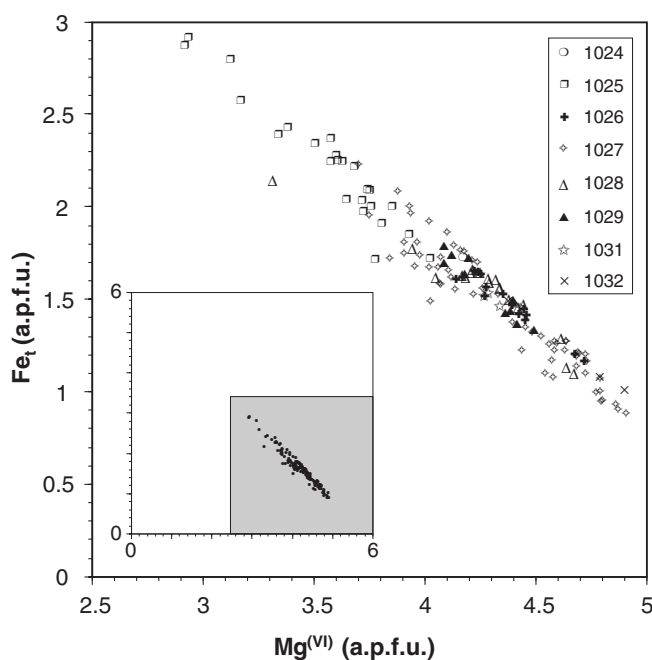


Figure 7. Plot of  $Mg^{VI}$  vs.  $Fe_t$  contents (a.p.f.u.) in octahedral sites of saponites. The inset shows the extent of the Mg- $Fe_t$  substitution in octahedral sites. a.p.f.u. = atoms per formula unit.

veins and vesicles, and also forms as a replacement of olivine, pyroxene, and plagioclase. The vein widths vary from about 0.5 to 2 mm. Crosscutting relationships with respect to clay veins and haloes surrounding clay veins indicate that the carbonate minerals generally occur late in the alteration sequence. Similarly, textures commonly indicate that aragonite formed earlier than calcite, and in many cases was actually replaced by calcite. The temperatures of present-day water-rock interaction at sites with evidence of carbonate mineralization range from Site 1025 at 35°C to Sites 1026–1027 at 63°C.

Chemical analyses of calcite and aragonite exhibit systematic differences (Table 5; Yatabe et al., Chap. 11, this volume). Calcites contain appreciable  $MgCO_3$ ,  $MnCO_3$ , and  $FeCO_3$ , as well as Ni, Cu, Zn, La, Ce, and Pb, whereas aragonites are relatively poor in these constituents. Relative to calcites, however, aragonites are enriched in Sr and Rb. These element distributions partly reflect crystal structural effects (Yatabe et al., Chap. 11, this volume).

### Sulfides

Secondary sulfides occur as minor or trace constituents at all sites. They are present as fine-grained euhedral to subhedral crystals disseminated in open fracture surfaces, fine grains within altered mesostasis, and as veinlets and vesicle linings. Sulfides are commonly associated with Fe-rich saponite and, when present, with carbonates. Most of the sulfide occurrences correspond to pyrite and subordinately to pyrrhotite; to date, the very subordinate occurrences of chalcopyrite and millerite are of unknown origin (e.g., secondary alteration, igneous, deuteric?).

### Talc, Quartz, and Zeolites

The presence of talc has been revealed by XRD analyses in samples from Sites 1026–1028 and 1032. It occurs almost exclusively as colorless to pale tan fibrous aggregates within pseudomorphic replacement of olivine together with Fe-rich saponites, or as the last product in the sequential fillings of fractures.

Quartz has been revealed by XRD analyses of two clay-bearing veins from Sites 1027 and 1032, but its presence was not confirmed by optical examinations under microscope.

Trace amounts of undifferentiated zeolites and phillipsite occur as colorless fibrous radiating aggregates in veinlets, mainly crosscutting the glassy rims of pillows, from Sites 1025 to 1032. Their presence has been confirmed by single crystal or separated aggregates X-ray analyses (with a Gandolfi Camera). Undifferentiated zeolites are present in significant amounts only in the hyaloclastite breccia from Hole 1026B (Section 168-1026B-3R-1) in the saponite-carbonates-bearing matrix.

## ALTERATION STYLE

In both younger and older pillow units, the alteration processes are mainly controlled by primary textural and structural features (i.e., the presence of impermeable glassy rims, the primary concentric structural zonation, and the vesicularity) and by the presence of radial, or irregularly distributed, fractures that crosscut the pillows from the outer glassy zone to the holocrystalline interior. Three main alteration environments with different degrees of alteration and secondary products have been distinguished: (1) alteration of glassy rims, (2) massive alteration along and around fractures (oxidation halos), and (3) pervasive alteration through diffusion.

### Alteration of Glassy Rims

The degree and the style of the glass alteration are strictly related to the presence of concentric and radial veins, which often form a complex network. The large set of veins crosscutting the glassy zone can be grouped in two main types on the basis of structural evidence: simple veins (Fig. 9A) and composite veins (Fig. 9B).

#### Simple Veins

The simple veins (<0.1–0.5 mm) characterize the glassy rims of pillow basalts from all nine sites. They show a distinct symmetric layering, parallel to the original crack (Pl. 1; Fig. 3), characterized by sharp compositional and mineralogical variations (Fig. 9A). Where a complete layering is developed, three distinct layers are present, and they are characterized (respectively from the outer to the inner part) by brown undifferentiated palagonite, a dark brown intimate mixture of K-bearing clays and Fe-oxyhydroxides, and greenish brownish fibrous to granular cryptocrystalline Mg-rich smectites. In the adjoining selvages the alteration of the glass usually proceeds from (1) fibrous form, around cracks and veins, (2) to a mottled texture within the glass, and (3) to extensive areas of yellow-brown palagonite between the varioles in the variolitic zone.

#### Composite Veins

The composite veins (2–5 mm) characterize samples from Sites 1206 and 1027 and developed as a consequence of repeated opening and crack filling along the median line of the primitive simple veins. The infilling secondary minerals are commonly symmetrically arranged, from the walls to the core of the vein, in the following sequence (Fig. 9B): (1) fibrous Mg-rich smectites, (2) fibrous radiating zeolites (mainly phillipsite), and (3) fibrous to blocky anhedral carbonates (calcite and aragonite).

#### Hyaloclastite Breccia

The hyaloclastite breccias of Hole 1026B represent an exaggerated example of glass alteration; the glass shards smaller than 1 mm are generally completely altered to undifferentiated palagonite, whereas

Table 4. Representative analyses of celadonite and celadonite-bearing mixtures.

Hole:	1024B	1024B	1024B	1024B	1026C	1026C	1026C	1026C	1026C	1027C	1027C	1029A	1029A	1029A	1031A	1031A	1031A	1032A	1032A
Core, section:	18X-CC	18X-CC	18X-CC	18X-CC	16R-1	17R-1	17R-1	17R-1	17R-1	3R-2	3R-2	25X-4	25X-4	25X-4	6X-1	6X-1	6X-1	12R-1	12R-1
Interval (cm):	10-37	10-37	10-37	10-37	40-45	13-17	13-17	13-17	13-17	115-117	115-117	7-12	7-12	7-12	49-52	49-52	49-52	126-132	126-132
Piece:	1	1	1	1	20	4	4	4	4	-	-	2	2	2	10	10	10	19	19
Depth (mbsf):	167.83	167.83	167.83	167.83	238.9	238.63	238.63	238.63	238.63	606.25	606.25	221.14	221.14	221.14	41.79	41.79	41.79	291.46	291.46
SiO <sub>2</sub>	50.63	49.05	48.12	49.93	49.16	51.56	48.32	49.02	50.73	49.01	46.48	52.89	50.43	51.46	47.63	48.91	49.16	49.25	49.30
TiO <sub>2</sub>	0.00	0.00	0.00	0.02	0.00	0.00	0.09	0.00	0.10	0.00	0.02	0.12	0.13	0.40	0.14	0.16	0.09	0.05	0.08
Al <sub>2</sub> O <sub>3</sub>	1.48	2.76	2.23	3.13	5.50	2.11	5.49	2.57	5.82	2.94	4.16	2.54	2.67	3.41	4.76	5.31	3.51	2.62	2.45
Cr <sub>2</sub> O <sub>3</sub>	0.04	0.02	0.03	0.08	0.01	0.02	0.02	0.00	0.09	0.00	0.00	0.00	0.00	0.00	0.00	0.00	0.00	0.00	0.00
FeO	28.55	26.91	29.34	27.74	23.30	24.74	23.93	25.71	23.39	27.54	26.60	26.53	26.24	25.93	27.80	27.53	30.15	27.53	27.02
MgO	3.20	3.34	2.58	3.92	3.71	4.92	3.16	3.27	4.25	3.10	2.76	3.77	3.29	3.48	2.38	2.57	2.55	4.12	3.21
MnO	0.09	0.00	0.00	0.00	0.13	0.03	0.00	0.02	0.07	0.00	0.11	0.18	0.10	0.18	0.11	0.06	0.07	0.15	0.12
NiO	0.09	0.42	0.10	0.10	0.00	0.00	0.00	0.00	0.06	0.00	0.05	0.63	0.13	0.19	0.07	0.11	0.21	0.10	0.10
CaO	0.87	1.01	1.15	0.87	0.74	0.42	0.70	0.53	1.14	1.34	1.51	1.37	0.86	1.36	1.15	1.13	1.12	1.42	1.21
Na <sub>2</sub> O	0.00	0.00	0.00	0.00	0.00	0.00	0.00	0.00	0.00	0.00	0.00	0.00	0.00	0.00	0.00	0.00	0.00	0.00	0.00
K <sub>2</sub> O	6.24	6.11	4.99	6.67	6.63	7.59	6.68	7.06	6.69	7.24	7.05	5.17	5.53	5.69	6.35	6.28	5.58	5.61	6.99
Total	91.19	89.62	88.54	92.46	89.18	91.39	88.39	88.18	92.34	91.17	88.74	93.20	89.38	92.10	90.39	92.06	92.44	90.85	90.48
Si	8.093	7.946	7.954	7.856	7.826	8.090	7.803	8.045	7.778	7.875	7.691	8.098	8.083	7.983	7.698	7.705	7.800	7.870	7.953
Al <sup>(IV)</sup>	0.000	0.054	0.046	0.144	0.174	0.000	0.197	0.000	0.222	0.125	0.309	0.000	0.000	0.017	0.302	0.295	0.200	0.130	0.047
Al <sup>(VI)</sup>	0.372	0.473	0.388	0.436	0.858	0.570	0.848	0.588	0.829	0.431	0.503	0.655	0.670	0.607	0.605	0.691	0.456	0.363	0.419
Fe <sub>t</sub>	3.817	3.646	4.056	3.650	3.102	3.246	3.232	3.529	2.999	3.701	3.681	3.397	3.517	3.364	3.758	3.627	4.000	3.679	3.645
Mg	0.762	0.806	0.636	0.919	0.880	1.151	0.761	0.800	0.971	0.742	0.681	0.860	0.786	0.805	0.573	0.603	0.603	0.981	0.772
Ti	0.000	0.000	0.000	0.002	0.000	0.000	0.011	0.000	0.012	0.000	0.002	0.014	0.016	0.047	0.017	0.019	0.011	0.006	0.010
Cr	0.005	0.003	0.004	0.010	0.001	0.002	0.003	0.000	0.011	0.000	0.000	0.000	0.000	0.000	0.000	0.000	0.000	0.000	0.000
Mn	0.012	0.000	0.000	0.000	0.018	0.004	0.000	0.003	0.009	0.000	0.015	0.023	0.014	0.024	0.015	0.008	0.009	0.020	0.016
Ni	0.012	0.055	0.013	0.013	0.000	0.000	0.000	0.000	0.007	0.000	0.007	0.078	0.017	0.024	0.009	0.014	0.027	0.013	0.013
Total	4.980	4.983	5.097	5.028	4.858	4.884	4.842	4.874	4.827	4.874	4.886	4.915	4.921	4.823	4.960	4.943	5.096	5.057	4.866
Ca	0.149	0.175	0.204	0.147	0.126	0.071	0.121	0.093	0.187	0.231	0.268	0.225	0.148	0.226	0.199	0.191	0.190	0.243	0.209
Na	0.000	0.000	0.000	0.000	0.000	0.000	0.000	0.000	0.000	0.000	0.000	0.000	0.000	0.000	0.000	0.000	0.000	0.000	0.000
K	1.272	1.263	1.052	1.339	1.346	1.519	1.376	1.478	1.308	1.484	1.488	1.010	1.131	1.126	1.309	1.262	1.129	1.144	1.438

Notes: Formulas have been calculated on the basis of 20 oxygens and four hydroxyls considering  $(\text{Si} + \text{Al})^{\text{IV}} = 8$  a.p.f.u. No normalizations have been performed for the octahedral sites.

the largest clasts (1–6 mm) show a concentric zonation, and the extent of alteration decreases from rim toward the center (where sometimes unaltered isotropic glass is preserved; Fig. 9C). Clasts are cemented by a polymineralic matrix mainly consisting of the same mineral assemblages observed in the composite veins.

**Chemical Variation in Altered Glass**

To define the major chemical variations during the alteration processes of glass crosscut by simple and composite veins, chemical analyses were performed by SEM-EDS. Chemical profiles indicate large variations between the four recognized zones (Fig. 10) in good

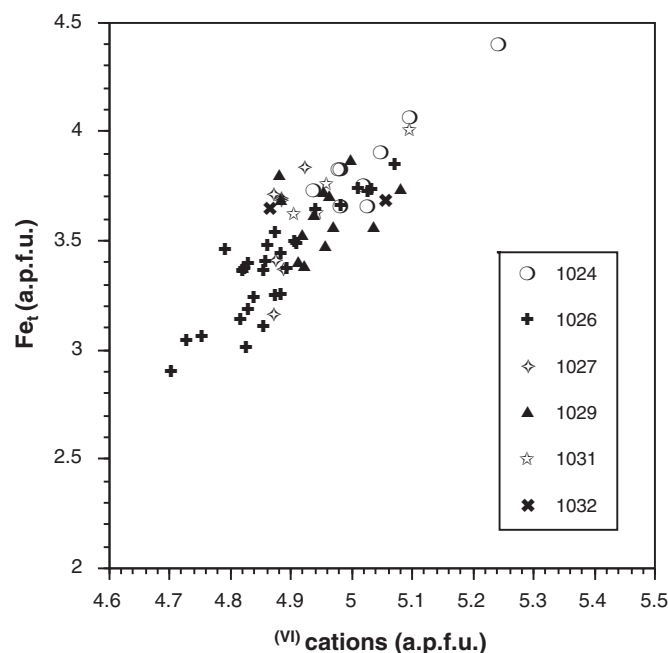


Figure 8. Plot of the total octahedral occupancy vs. Fe<sub>t</sub> contents (a.p.f.u.) of celadonite and celadonite-bearing mixtures. a.p.f.u. = atoms per formula unit.

agreement with textural and mineralogical observations (Fig. 9). The outer brown zone (Zone 4; Fig. 10), which represents the less evolved glass alteration, shows significant gains in K<sub>2</sub>O, SiO<sub>2</sub>, and Al<sub>2</sub>O<sub>3</sub>. In contrast Fe<sub>2</sub>O<sub>3</sub>, MgO, CaO, and Na<sub>2</sub>O are strongly depleted (the last two elements remaining unchanged toward the central part of the vein). In the intermediate layer (Zone 3; Fig. 10), the strong enrichment of Fe<sub>2</sub>O<sub>3</sub> and K<sub>2</sub>O is related to the formation of authigenic phases such as alkali-bearing clays (celadonite) and Fe-oxyhydroxides. The chemistry of the central part (Zones 2 and 1; Fig. 10) agrees well with the composition of the observed smectites, and no major variations between fibrous and cryptocrystalline granular part are evident. The chemical profiles across the altered glass around the composite veins and across the hyaloclastic fragments are generally comparable.

The composition of altered glass relative to the three main zones (from both vein types) normalized vs. the composition of the adjoining unaltered glass allows the evaluation of a general chemical balance for the fluid–glass interaction during the veining processes (Fig. 11). The major variations involve the increase of H<sub>2</sub>O and K<sub>2</sub>O, the strong loss of Na<sub>2</sub>O and a minor but significant depletion of CaO and MnO<sub>t</sub>. Total Fe<sub>2</sub>O<sub>3</sub>, MgO, NiO, and Cr<sub>2</sub>O<sub>3</sub> show minor and comparable degrees of depletion, whereas SiO<sub>2</sub> and Al<sub>2</sub>O<sub>3</sub> remain almost unchanged.

**Massive Alteration Along and Around Fractures in Hypocrystalline and Holocrystalline Pillows Interiors**

The fracture systems that characterized almost all the analyzed pillow basalts represent the most important channel ways for the fluid circulation within the pillow units and consequently the preferential sites where fluid–rock interaction starts and develops into the adjoining rock. Fluid–rock interaction generates monomineralic or polymineralic coatings or fillings within fractures and variably sized oxidation halos in the adjoining selvages.

**Veins**

Several vein types and generations have been recognized throughout all Leg 168 pillow basalts (individual occurrences are recorded in the VEINLOG; see Appendix D of the Leg 168 *Initial Reports*; Davis, Fisher, Firth, et al., 1997).

**Table 5. Representative analyses of carbonates.**

Hole:	1027C	1027C	1027C	1027C	1028A	1028A	1028A	1028A	1028A	1028A	1032A	1032A	1032A	1032A
Core, section:	5R-5	5R-5	5R-5	5R-5	15X-7	15X-7	15X-7	15X-7	15X-7	15X-7	12R-1	12R-1	12R-1	12R-1
Interval (cm):	22-27	22-27	22-27	22-27	15-18	15-18	15-18	15-18	15-18	15-18	126-132	126-132	126-132	126-132
Piece:	2	2	2	2	2	2	2	2	2	2	19	19	19	19
Depth (mbsf):	628.95	628.95	628.95	628.95	132.89	132.89	132.89	132.89	132.89	132.89	291.46	291.46	291.46	291.46
Texture	Massive	Massive	Fibrous	Fibrous	Fibrous	Fibrous	Fibrous	Massive	Massive	Massive	Fibrous	Fibrous	Fibrous	Columnar
FeCO <sub>3</sub>	2.338	2.322	0.452	0.968	0.177	0.144	0.064	0.113	0.127	0.159	0.097	0.258	0.258	0.364
MnCO <sub>3</sub>	14.438	14.098	0.875	1.199	0.275	0.193	0.000	0.048	0.064	0.112	1.507	1.961	1.815	8.806
MgCO <sub>3</sub>	8.221	8.577	0.126	1.946	0.000	0.000	0.000	0.000	0.000	0.000	0.000	0.000	0.000	0.000
CaCO <sub>3</sub>	71.783	70.784	97.984	94.718	98.930	99.445	99.496	99.366	99.546	99.653	98.162	97.645	97.930	91.954
BaCO <sub>3</sub>	0.193	0.360	0.219	0.309	0.232	0.230	0.076	0.242	0.177	0.089	0.167	0.206	0.064	0.139
SrCO <sub>3</sub>	0.028	0.000	0.000	0.000	1.781	1.316	1.488	0.310	0.084	0.183	0.000	0.000	0.000	0.000
Total	97.001	96.141	99.656	99.140	101.395	101.329	101.123	100.079	99.998	100.195	99.933	100.069	100.067	101.264
FeCO <sub>3n</sub>	2.410	2.415	0.453	0.976	0.175	0.142	0.063	0.113	0.127	0.159	0.097	0.258	0.258	0.359
MnCO <sub>3n</sub>	14.884	14.663	0.878	1.210	0.272	0.191	0.000	0.048	0.064	0.112	1.508	1.959	1.814	8.697
MgCO <sub>3n</sub>	8.475	8.921	0.126	1.962	0.000	0.000	0.000	0.000	0.000	0.000	0.000	0.000	0.000	0.000
CaCO <sub>3n</sub>	74.002	73.625	98.323	95.541	97.568	98.141	98.391	99.288	99.548	99.459	98.228	97.577	97.864	90.807
BaCO <sub>3n</sub>	0.199	0.375	0.220	0.312	0.228	0.227	0.075	0.242	0.177	0.089	0.167	0.206	0.064	0.137
SrCO <sub>3n</sub>	0.029	0.000	0.000	0.000	1.756	1.299	1.471	0.310	0.084	0.182	0.000	0.000	0.000	0.000
Total	100.000	100.000	100.000	100.000	100.000	100.000	100.000	100.000	100.000	100.000	100.000	100.000	100.000	100.000
Fe <sup>2+</sup>	0.042	0.042	0.008	0.017	0.003	0.002	0.001	0.002	0.002	0.003	0.002	0.004	0.004	0.006
Mn <sup>2+</sup>	0.261	0.257	0.015	0.021	0.005	0.003	0.000	0.001	0.001	0.001	0.026	0.034	0.032	0.153
Mg <sup>2+</sup>	0.203	0.213	0.003	0.047	0.000	0.000	0.000	0.000	0.000	0.000	0.000	0.000	0.000	0.000
Ca <sup>2+</sup>	1.492	1.484	1.972	1.912	1.966	1.974	1.978	1.991	1.994	1.992	1.970	1.959	1.963	1.839
Ba <sup>2+</sup>	0.002	0.004	0.002	0.003	0.002	0.002	0.001	0.002	0.002	0.001	0.002	0.002	0.001	0.001
Sr <sup>2+</sup>	0.000	0.000	0.000	0.000	0.024	0.018	0.020	0.004	0.001	0.002	0.000	0.000	0.000	0.000
Total	2.000	2.000	2.000	2.000	2.000	2.000	2.000	2.000	2.000	2.000	2.000	2.000	2.000	2.000

Notes: XCO<sub>3n</sub> = carbonate analyses normalized to 100%. Formulas have been calculated on the basis of six oxygens per unit cell.

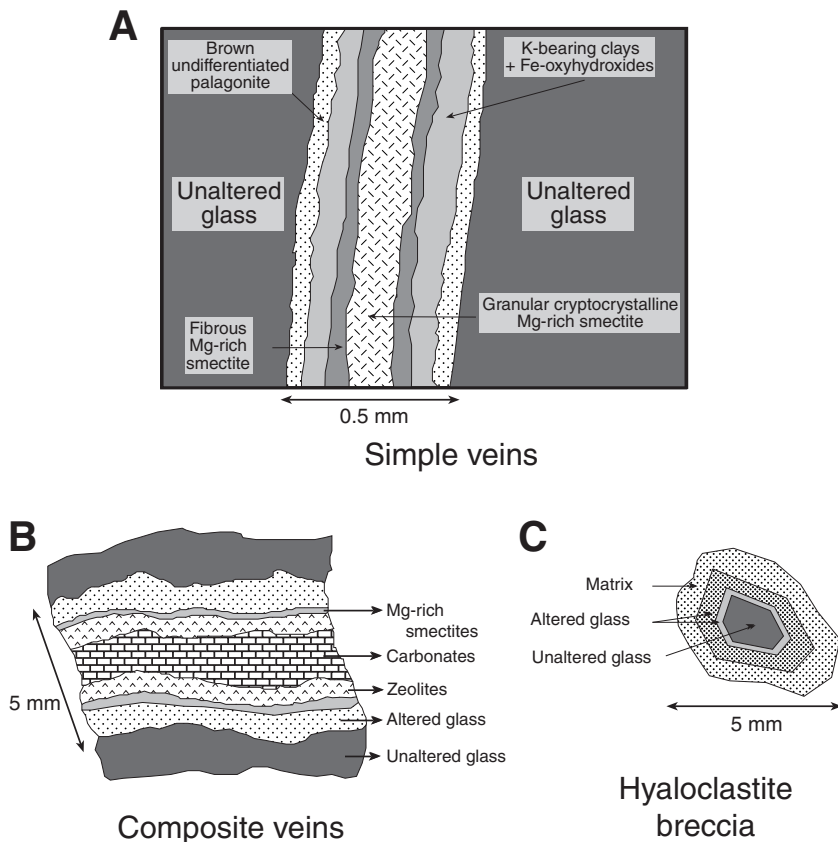


Figure 9. Sketch of various glass alteration features. **A.** Simple vein (sketched from Pl. 1, Fig. 3; Sample 168-1027C-1R-6, 67–70 cm [Piece 2]). **B.** Composite veins (Sample 168-1027C-1R-6, 67–70 cm [Piece 2]). **C.** Glassy shard from hyaloclastite breccia of Hole 1026B (Sample 168-1026B-3R-1, 18–25 cm [Piece 3]).

We distinguish three main vein types on the basis of their geometric relationships: concentric veins, radial veins, and irregular veins. Most of the concentric and radial veins presumably represent filled shrinkage cracks that increase in frequency toward quenched surfaces. Irregular veins can be alternatively explained as filled shrinkage cracks variably distributed and oriented as a consequence of mechanical and lithological heterogeneities, or as secondary fractures developed in the “cold” rock during later spreading-related tectonism.

The concentric veins (<0.1–0.5 mm thick) are mainly concentrated in the glassy zone and subordinately in the outer hypocrySTALLINE pillow zones, whereas radial and most of the irregular veins (<0.1–5 mm thick) crosscut the pillows from the outer glassy rims to the holocrystalline interior.

The mineralogical composition of the veins is extremely variable from site to site and in many cases strong variations occur even at the scale of the single sample. Nevertheless, two main vein types can be distinguished on the basis of the mineralogic assemblages of the filling products: veins characterized by oxidizing filling assemblages (V1) and veins characterized by reducing filling assemblages (V2).

V1 are common in pillow basalts from every site and are characterized by the following mineral assemblages, characteristic of the oxidizing style of alteration (as defined by Andrews, 1980): hematite, goethite, iddingsitic mixtures (Types 6–9; Table 2), celadonic minerals (Types 3–5; Table 2), and Mg-rich saponites (Type 2; Table 2). These minerals are commonly arranged in submillimetric to millimetric symmetric layers, parallel to the original crack. In many cases, the transition between the different layers is graded and each layer progressively fades out toward the adjacent, suggesting dynamic growth with a progressive variation of the chemical conditions (Eh and pH) of the microenvironment. Although some exceptions have been recognized, the temporal depositional sequence can be summarized as follows: (1) Fe-oxides and Fe-oxyhydroxides and/or iddingsitic mixtures, (2) celadonic minerals, and (3) Mg-rich saponites. The commonest variation from this general trend is the inversion between 1 and 2.

V2 have been recognized only in pillow basalts from Sites 1027, 1028, and 1032, and are characterized by “nonoxidative” mineral assemblages (Andrews, 1980) mainly represented by carbonates after Fe-rich saponite (Type 1; Table 2). Sulfides (mainly pyrite) are irregularly distributed within this assemblage but mainly occur in the outer rims of the veins associated with saponite. In some cases, especially in veins from Sites 1027 and 1032, up to three generations of carbonates occur varying in texture and composition, from the rims to the median line of the vein. Columnar crystals, often deformed, commonly characterize the outer rims, after fibrous radiating sheaf, whereas the central part commonly displays a blocky arrangement of undeformed anhedral to subhedral crystals. Together with this textural variation, carbonates vary from almost pure aragonite (commonly intimately intergrown with saponite) to Mn-, Mg-, and Fe-bearing calcite (respectively,  $\text{MnCO}_3 \leq 15$  mol%,  $\text{MgCO}_3 \leq 9$  mol%, and  $\text{FeCO}_3 \leq 3$  mol%) in the fibrous and columnar part of the vein. The blocky central part is often affected by recrystallization processes and is commonly characterized by almost pure calcium carbonates (mainly calcite). A significant example of the chemical variations in carbonates of the three generations is reported in Figure 12 relative to Sample 168-1032A-12R-1, 9–16 cm (Piece 1).

In several cases from Sites 1027 and 1032 there is evidence that V2 mostly developed as a consequence of repeated opening and crack filling along the median line of the early celadonite + iddingsite  $\pm$  Mg-rich saponite veins (V1). This is clearly shown by the presence of V1 millimetric fragments (mainly iddingsite and celadonite) arranged in regular trails running parallel to the vein walls along the central part of the V2 (i.e., within the blocky calcite).

#### Oxidation Halos

Oxidation halos are present around V1 fractures and veins in pillow basalts from every site (with maximum abundance in samples from Sites 1026, 1027, 1029, and 1032) and are typically absent around V2 veins. These halos are a few millimeters to several centi-

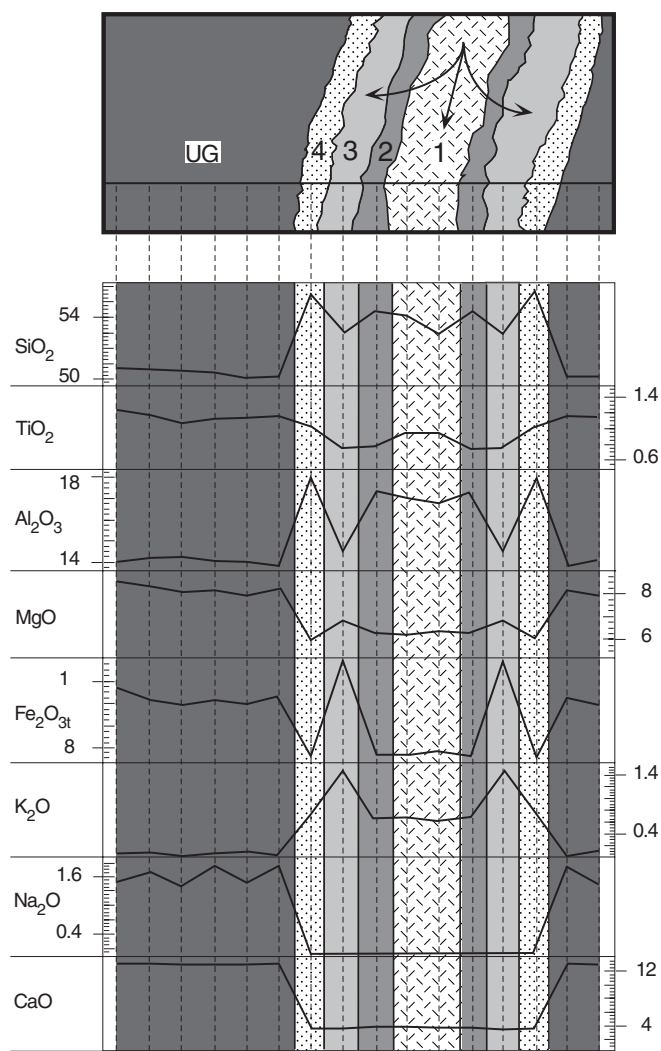


Figure 10. Major chemical variations across alteration layers (Zones 1–4 as described in the text) in the simple vein sketched in Figure 9A. UG = unaltered glass.

meters thick and appear in hand specimens as dark borders on rock pieces that may be stained with orange or yellow. The percentage of the observed halos always decreases progressively from the outer quenched margin to the holocrystalline pillows interior. In every studied sample, oxidation halos always represent the zone of most intense alteration with respect to the nonhalo portions of the rock. Microscopic observations allow the recognition of three main types of alteration zones that, when present together, show the following spatial and temporal relationships (Fig. 13): reddish brown zone (RZ), greenish red to green zone (GZ), and greenish to light gray zone (TZ). The black halos found by other authors in pillow basalts from various oceanic settings (Böhlke et al., 1980, 1981, 1984; Alt and Honnorez, 1984; Alt et al., 1996; Buatier et al., 1989; Laverne et al., 1996) were not recognized in the studied samples.

**RZ**

The reddish brown zone (1–5 mm thick) always occurs immediately around fractures or veins of Type 1 (V1) and is characterized by a massive precipitation of secondary minerals, mainly represented by goethite, hematite, undifferentiated Fe-oxyhydroxides, iddingsitic mixtures, and subordinately by celadonite and celadonite-bearing

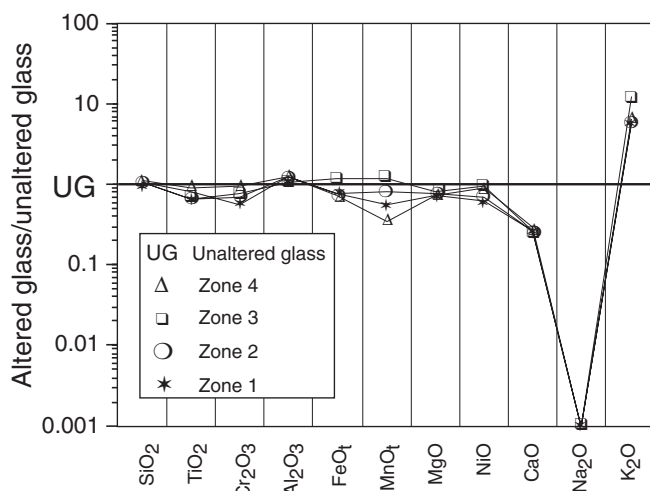


Figure 11. Composition of altered glass across alteration layers (Zones 1–4 as in Fig. 10) normalized to the adjoining unaltered glass.

mixtures. Partial or complete oxidation of titanomagnetite to titanomaghemite is also common, especially in samples from Site 1029. RZ are always more extensively altered than the other adjacent zones and the total amount of alteration, determined by point counting the secondary minerals in thin section, varies from 30% to 50% with maximum values variable between 50% and 60% in some samples from Site 1027. Secondary phases, often showing complex temporal and spatial relationships, occur as vesicles or miarolitic void fillings, pseudomorphic replacement of mafic minerals (mainly olivine), and irregular patches or disseminated aggregates within mesostasis. A statistical study of the mineralogical zonation of the vesicle fillings (Fig. 13A) shows that, despite some exceptions recognized in every site, the most common sequence of mineral formation in RZ is the following: (1) goethite or undifferentiated Fe-oxyhydroxides cryptocrystalline aggregates, (2) hematite lamellae, (3) iddingsite, (4) iddingsite-bearing mixtures, and (5) celadonite or celadonite-bearing mixtures. This temporal and spatial sequence agrees well with that observed within the adjacent veins (Fig. 13B).

**GZ**

The greenish red to green zone (1–2 mm thick) is located immediately adjacent to RZ and occurs systematically only in samples from Sites 1026, 1027, 1029, and 1032. The total amount of alteration varies from 30% to 40%, and secondary phases occur as in the reddish brown zone previously described. The most common minerals are celadonite and celadonite-bearing mixtures (both with iddingsite and Mg-rich saponite) associated with an extremely variable amount of iddingsite, Fe-oxyhydroxides, and subordinate amounts of Mg-rich saponite (Type 2; Table 2). The sequence of the alteration inferred by the most common mineralogical zonation of the vesicle fillings (Fig. 13A) suggests that celadonite and celadonite-bearing mixtures occur, in most of the cases, after Fe-oxyhydroxides and iddingsite. When present, the last phase to form is the Mg-rich saponite.

**TZ**

The greenish to light gray zone (1–3 mm thick) represents the transition between the oxidation halos and the nonhalo portion of the rock. It represents the zone with the most complicated spatial and temporal relationships between the different secondary phases, which are represented by celadonite, celadonite-bearing mixtures, Mg-rich saponite, Fe-rich saponite, and minor iddingsite. The alteration intensity is extremely heterogeneous, even at the scale of the single sample, and varies from <10% to about 30%. A temporal and

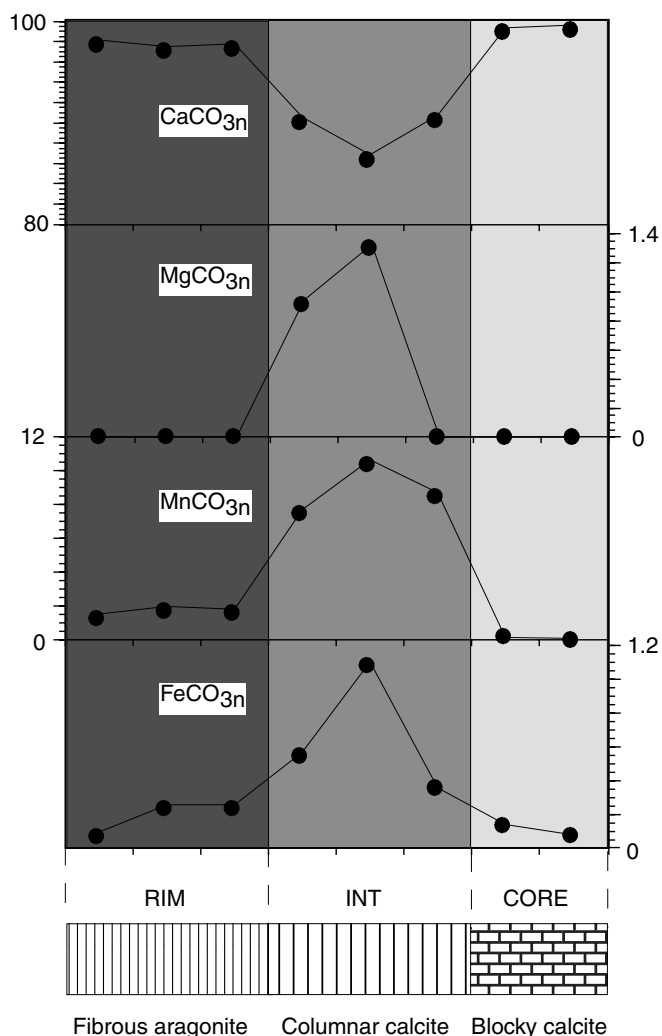


Figure 12. Compositional variations in carbonates of the three different generations recognized across a V2 vein (Sample 168-1032A-12R-1, 9–16 cm [Piece 1]).  $XCO_{3n}$  = carbonate analyses normalized to 100%.

spatial sequence of secondary mineral formation representative of all studied samples is very difficult to identify. Nevertheless the following switched sequences are two of the most common that were observed (Fig. 13A): (A) iddingsite → celadonite → Mg-rich saponite → Fe-rich saponite; and (B) Fe-rich saponite → Mg-rich saponite → celadonite → iddingsite. Sequences (A) and (B) can be repeated more than one time even in the same vesicle. The complex relationships between secondary phases of this zone can be explained as the result of local equilibrium variations of the microenvironment that presumably occurred during the transition from the oxidizing alteration, in a water-dominated system, to the reducing alteration in a rock-dominated system.

Because oxidation halos flank only V1 veins and fractures and are typically absent around later V2 carbonate-bearing veins (Fig. 13B), it seems that they have developed early and always before the reducing alteration marked by the pervasive precipitations of Fe-rich saponites, carbonates, and sulfides in the gray interior (Fig. 13). The concentric configuration and the sharp boundaries between the different zones within the halos suggest that they developed under the control of diffusion from the solutions that occupied the fractures, which penetrated into the rock roughly perpendicular to the original fractures. Because the alteration products are mainly represented by Fe-

oxyhydroxides and K-bearing clays, it is likely that the alteration phase related to the formation of the halos is triggered by normal or slightly evolved seawater.

### Pervasive Alteration Through Diffusion

The gray rocks that are unaffected by oxidation halos show a degree of alteration and a secondary mineralogy extremely variable from site to site. Generally their alteration intensity increases systematically with the distance from the ridge axis (i.e., from younger to older pillow basalts). The only exception is represented by the pillow basalts from Site 1028, which in some cases show a degree of alteration comparable to the oldest site drilled during Leg 168 (i.e., Site 1027).

In this portion of the pillow interior, the dominant mechanism that triggers the alteration processes is pervasive fluid seepage occurring primarily along the grain boundaries of the igneous minerals and primary voids. Alteration is mainly concentrated around phenocrysts, within gas and segregation vesicles, and miarolitic voids.

Fe-rich saponites and carbonates are the main secondary phases characterizing this stage of the alteration, but carbonates are completely absent in pillow basalts from Sites 1023 to 1025, 1029, and 1031. They both occur as pseudomorphic replacement of olivine (Pl. 1; Fig. 4) and sometimes of clinopyroxene, as dense patches within mesostasis, and as vesicle and fracture fillings and coatings in all the studied samples. Talc is a subordinate secondary product and has been recognized in Sites 1026 to 1028 and 1032, whereas sulfides are always a minor constituent. As evidenced by the spatial variations in vesicle and vein fillings (Fig. 13) and by the temporal relationships of the crosscutting veins, the carbonates seem to be always the last secondary minerals to form. The formation of talc suggests that a significant increase of Si activity occurred at Sites 1026 to 1028 and 1032 in the latest stages of alteration.

### FROM OXIDIZING TO REDUCING ALTERATION

The transition from alteration processes controlled by the presence of fractures to those related to the pervasive fluid seepage within the unfractured rock separates two different styles of alteration that respectively occur under oxidizing and reducing conditions. Although several exceptions exist, the most common mineral paragenesis characterizing the two styles of alteration are quite distinct and are in good agreement with those observed by numerous authors (e.g., Andrews 1977, 1980; Alt, Kinoshita, Stokking, et al., 1993; Laverne et al., 1996; Teagle et al., 1996): (1) assemblages under oxidizing conditions: Fe-oxyhydroxides ± iddingsite ± celadonite ± Mg-rich saponite; and (2) assemblages under reducing conditions: Fe-rich saponites ± carbonates ± sulfides ± talc.

Sensitive markers of the transition from assemblages 1 to 2 are the mineralogical and minerochemical variations involving the clay minerals, the mixed-layer clays, and the clay mixtures. As evidenced in Figure 14 (where the complete set of the analyzed secondary minerals is reported), good indicators of the major chemical variations are the  $K_2O$ ,  $FeO_T$ , and MgO contents of these secondary phases. Following the crystallization order in the polymineralic fillings of the gas vesicles from the different zones discussed in the previous section, it is possible to associate these chemical changes with the spatial and temporal variations occurring during the alteration processes.

As evidenced in Figure 15 (Steps 1–2) the most important variation occurring in the early stages of the oxidizing alteration (i.e., in the reddish brown and greenish halos) is the progressive decrease of Fe-rich minerals associated with the concomitant increase of K-bearing minerals and mixtures (i.e., Fe-oxyhydroxides → iddingsite → iddingsite-celadonite mixtures → celadonite-iddingsite mixtures → celadonite). Oxygen isotope data suggest temperatures up to 40°C

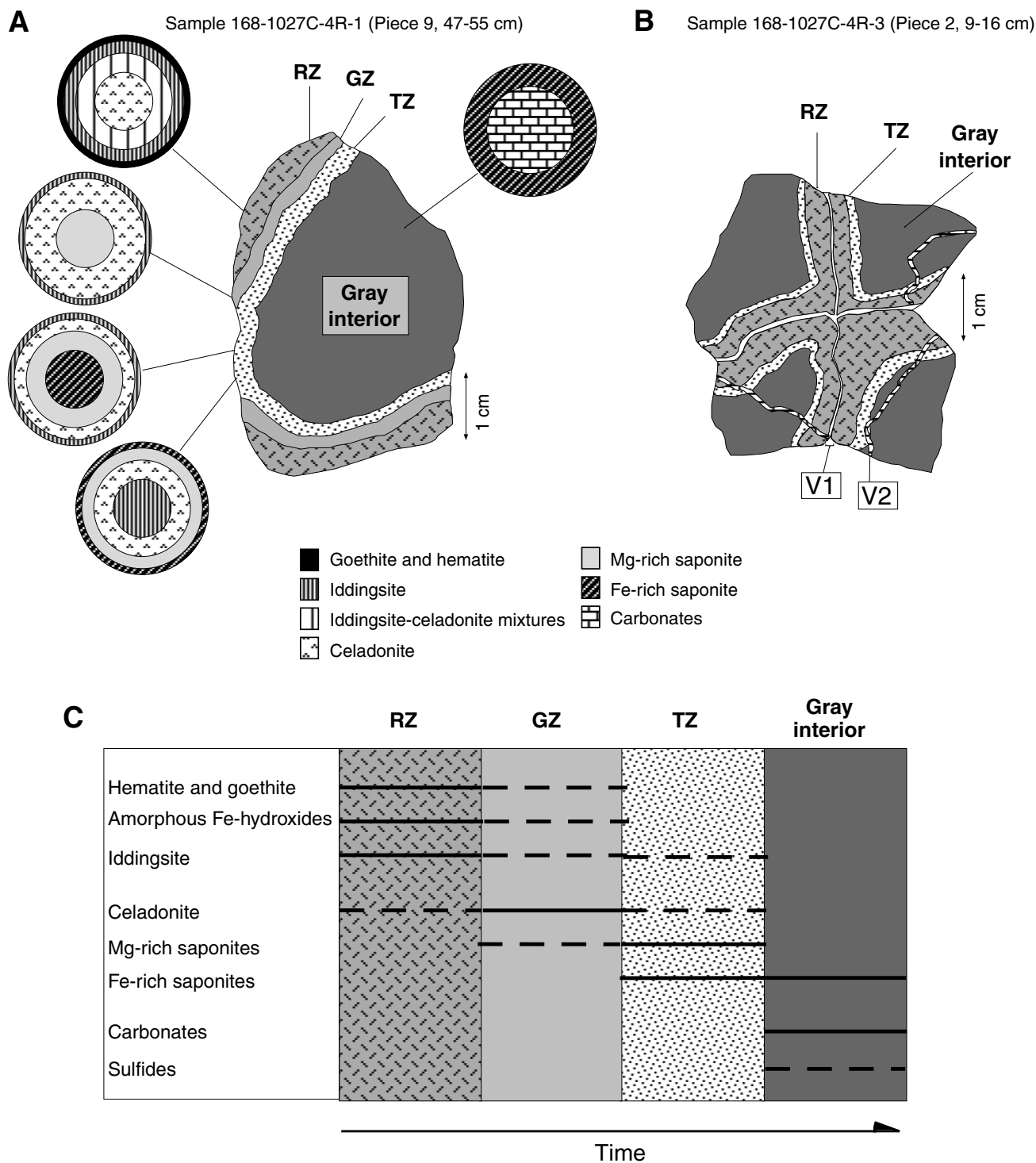


Figure 13. Sketches of alteration halos in two samples from Hole 1027C and secondary mineral distribution within the halos. **A.** Sequential vesicle linings in the four recognized zones. **B.** Geometric relationship between halos and veins. **C.** Temporal and spatial distribution of secondary minerals across halos zonations. RZ = reddish brown zone; GZ = greenish red to green zone; TZ = greenish to light gray transitional zone; V1 and V2 = vein types as described in the text.

for the formation of celadonite and celadonite-bearing mixtures (Kastner and Gieskes, 1976; Seyfred et al., 1978; Andrews, 1980; Böhlke et al., 1984). Consequently, this assemblage forms at very low temperatures, slight alkaline conditions, high oxidation potentials, and requires substantial supplies of Fe and K from the circulating fluids. All these constraints suggest that seawater is the fluid re-

sponsible for this early alteration stage. Nevertheless, although K is indigenous to normal seawater, significant amounts of iron are required to justify the massive precipitation of Fe-oxyhydroxides and iddingsite. Presumably iron is supplied to the circulating fluids in part by the breakdown of olivine and in part during the reaction that occurred in the fracture systems of the adjacent glassy rims.

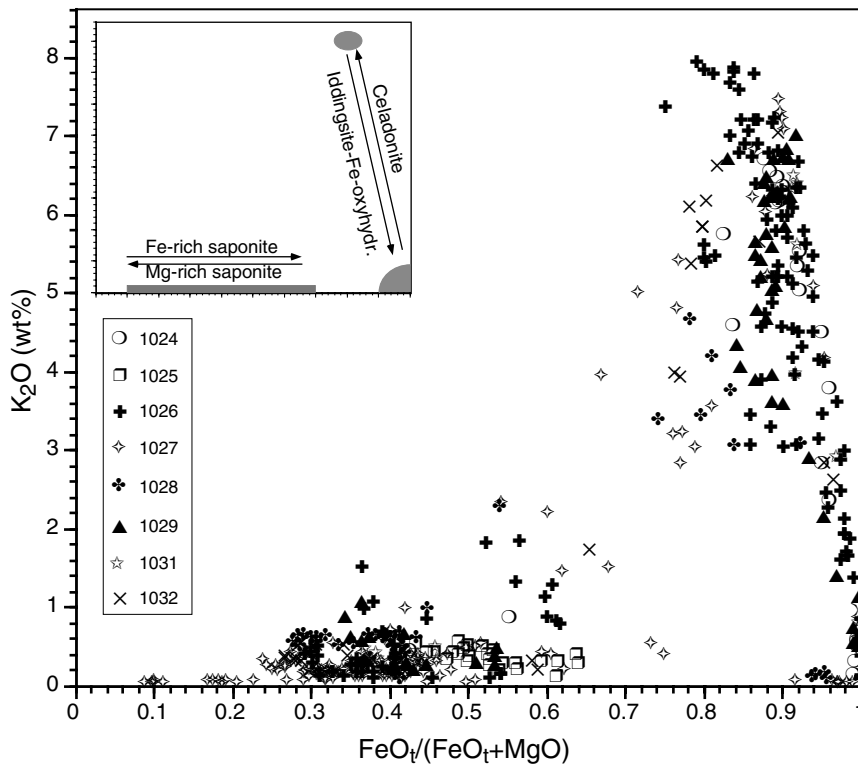


Figure 14. Plot of  $\text{FeO}_t/(\text{FeO}_t + \text{MgO})$  vs.  $\text{K}_2\text{O}$  of clays and clay mixtures. Arrows in the inset show the variation trend of mixtures or solid solutions between different phases.

The next stage of the alteration (Steps 2–3; Fig. 15) is recorded by the appearance of the Mg-rich saponite as the dominant secondary mineral. As discussed by Andrews (1980) the transition from Fe- and K-rich assemblages to Mg-rich saponite reflects a gradual and systematic extraction of oxygen from the circulating fluids during the progressive interaction with the host rock. The progressive change of the fluid chemistry is associated with a gradual closure of the main circulation pathways, which represents the first step of the transition from a fluid-dominated to a rock-dominated system.

The first growth of Fe-rich saponites, often associated with scattered but widespread sulfides, and the contemporaneous disappearance of secondary minerals that require high oxidation potential (such as iddingsite and celadonite) mark the transition to the reducing style of alteration (Steps 3–4; Fig. 15). The chemical variations from Mg- to Fe-rich saponites that are associated with this transition reflect a new increased availability of ferrous iron in the circulating fluids. This is presumably related to a significant decrease of Eh of the environment (at least in the region of sulfide stability), which allows iron to be removed from the host rock and mobilized in the fluid.

Nevertheless the complete data set of clay analyses from the present study and from other members of the ODP Leg 168 Scientific Party (Hunter et al., 1999; Porter et al., Chap. 12, this volume) seem to indicate that the variation of Fe and Mg content in saponite could also be related to the bulk rock chemistry of the basalts. In fact all saponites (both Mg rich and Fe rich) from Site 1025 and subordinately from Site 1029 (i.e., those present in fractionated ferrobasalt) always show the lower Mg/Fe<sub>t</sub> ratio when compared to the other occurrences (Fig. 7).

The last stage of the alteration begins with the first appearance of carbonates (Step 4–5; Fig. 15); this stage has been recognized only in samples from Sites 1025, 1027, 1028, and 1032. At the beginning an almost pure  $\text{CaCO}_3$  carbonate (in most of the cases aragonite; Yatabe et al., Chap. 11, this volume) clearly coprecipitated together with variable proportions of Fe-rich saponites in the outer rims of the vein. Subsequently, calcite with significant amounts of Mn and minor Fe and Mg became the dominant secondary phase. A third generation of

carbonates (almost pure  $\text{CaCO}_3$  calcite) has been recognized only in samples from Sites 1027 and 1032. This evidence suggests that while carbonates precipitated together with saponite, their dominant cation is  $\text{Ca}^{2+}$  with other cations being partitioned into the clay minerals. As the saponite became progressively a minor constituent, the composition of carbonates changed to include  $\text{Mn}^{2+}$ ,  $\text{Fe}^{2+}$ , and  $\text{Mg}^{2+}$ , along with  $\text{Ca}^{2+}$ . The source of bicarbonate necessary to achieve carbonate saturation in the fluid is not completely clear. One possible source is dissolution within the base of turbiditic sediments onlapping the pillow basalts. If this is so, then carbonates and some other phases related to the reducing stages of alteration occurred when the eastern flank of the JdFR became buried, and open circulation of seawater within the basement became restricted or absent.

Hunter et al. (1999) suggested temperatures of formation for the carbonates varying from about 35° to 70°C. As for the oxidizing stages of the alteration, these temperatures are in good agreement with those estimated at the present-day basement/sediment interface (Davis, Fisher, Firth, et al., 1997).

## SUMMARY AND CONCLUSIONS

Although samples from Leg 168 represent an incomplete record (partly because of the very low recovery rates at some sites; Davis, Fisher, Firth, et al., 1997), many indexes suggest that the alteration intensity of pillow basalts from Leg 168 systematically increases with the distance from the present-day ridge. This indicates that the aging of the igneous crust (i.e., the time available for secondary mineral growth) and the measured increase of temperatures at the sediment/basement interface, from the younger HT to the older RB Sites (from 15° to 64°C; Davis, Fisher, Firth, et al., 1997), play a very important role in the overall alteration processes. The observation of increased alteration with crustal age has also been reported for a 1.6-Ma transect through pillow basalts of the Blanco Fracture Zone located at a different latitude on the eastern flank of the JdFR (Juteau et al., 1995).

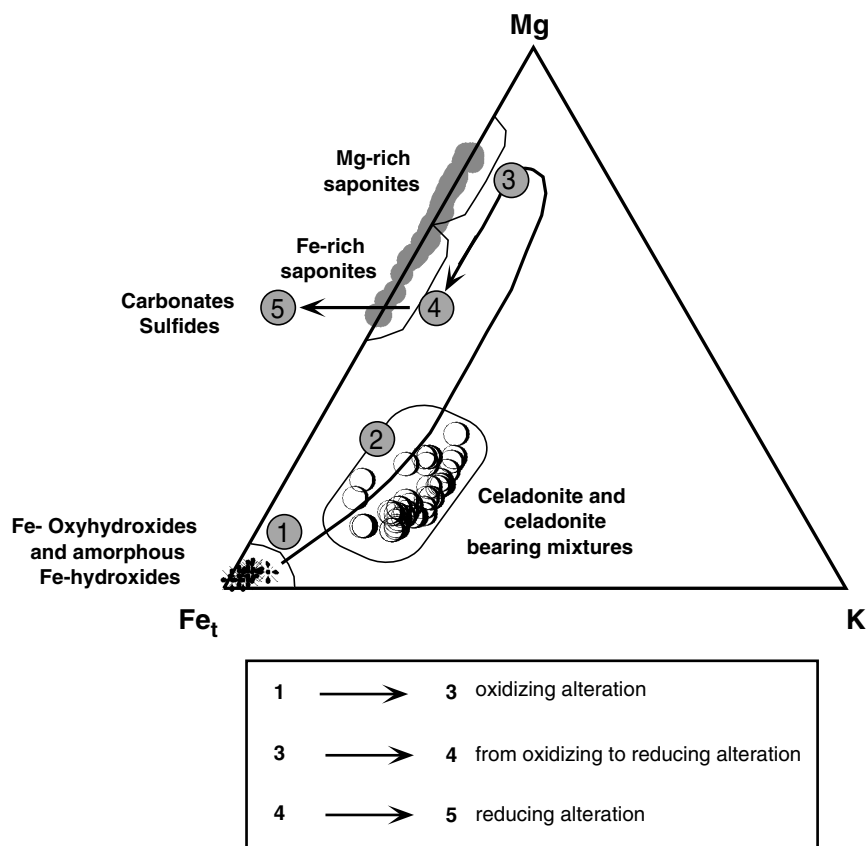


Figure 15. Fe<sub>t</sub>-K-Mg plot of clays and clay mixtures with the hypothesized evolution from oxidizing to reducing alteration.

Other important factors controlling the alteration intensity are the degree of fracturing of the pillow units and subordinately the local and regional variations in lithology and primary porosity (e.g., vesicularity, degree of crystallinity). Particularly, in both younger and older pillow units, the style of the alteration processes is mainly controlled by the presence of concentric and radial fractures, which crosscut all pillows from the outer glassy zone to the holocrystalline interior. Fractures are the most important pathways that allow significant penetration of fluids into the rock, controlling the alteration of the glassy rim and the early oxidizing stage of pillow alteration. In fact, most of the glassy margins of the pillow basalts recovered during ODP Leg 168 are unaltered or weakly altered except along and around concentric and radial cracks or veins.

The alteration of glass occurs in several different steps: (1) penetration of the fluids in the glass along the newly formed cracks allows the formation of a first generation of palagonite; (2) palagonite then evolves from amorphous brown patches to brownish yellow incipiently crystalline (sometimes fibrous) symmetric areas; and (3) palagonite is progressively replaced by dioctahedral clays (celadonite), Fe-oxyhydroxides, and trioctahedral smectites. More evolved glass alteration occurs in the oldest Sites 1026 and 1027, where a new veining stage is superimposed on the primary veins through repeated opening and crack filling processes along the median line of the original crack. Also in these cases the infilling secondary minerals are commonly symmetrically arranged and occur in the following sequence: (1) fibrous trioctahedral smectites, (2) fibrous radiating zeolites, and (3) fibrous to blocky anhedral carbonates. Most of the elements involved in the glass breakdown are used in, or immediately around, the vein to form secondary authigenic minerals. The strong enrichment in K<sub>2</sub>O from the circulating seawater allows the growth of dioctahedral clays (celadonite type) in the first step of alteration, whereas smectites, zeolites, and carbonates act as a sink for a significant portion of the removed Mg, Ca, Na, Al, and Si. Part of the leached iron is immediately used to form thin layers of Fe-oxyhydroxides

often associated with K- and Fe-bearing clay, whereas the remaining Fe and most of the Mn are removed from the glassy zone by the circulating fluids.

The hypocrystalline and holocrystalline portion of pillow basalts are characterized by two different styles of alteration that occur under oxidizing or reducing conditions. These alteration styles agree well with many studies performed on the alteration of other young pillow basalt sequences (Andrews, 1980; Böhlke et al., 1980, 1981; Alt, Kinoshita, Stokking, et al., 1993; Laverne et al., 1996). The most common mineral paragenesis characterizing the two style of alteration are well defined: (1) assemblages under oxidizing conditions: Fe-oxyhydroxides ± iddingsite ± celadonite ± Mg-rich saponite; and (2) assemblages under reducing conditions: Fe-rich saponite ± carbonates ± sulfides ± talc.

All the observed mineralogical and chemical variations occurring during the early stage of the alteration are interpreted as the result of rock interaction with “normal,” alkaline, and oxidizing seawater along preferential pathways represented by the concentric and radial crack systems. The chemical composition of the fluid progressively evolved while moving into the basalt leading to a reducing alteration stage, which is responsible for the precipitation of Fe-rich saponite and minor sulfides. The widespread aragonite/calcite formation represents the last stage of alteration that occurs as a consequence of the progressive saturation of the fluid with respect to carbonates. This stage probably occurred when the eastern flank of JdFR was completely buried by turbiditic sediments that hydrologically sealed the igneous crust and inhibited open seawater circulation within the igneous basement.

#### ACKNOWLEDGMENTS

This research was supported by the CNR (ODP-Italy) and by the “Ricerca di Ateneo” grants (Università degli Studi di Genova). We

wish to thank the Master, Crew, and Scientific Party of Leg 168 for the wonderful cooperation. We thank L. Cortesogno and G. Lucchetti for the helpful discussion. We also thank L. Negretti (SEM technician, Università di Genova) and A. Cucchiara (XRD technician, Università di Genova) for their invaluable analytical help. P.M. thanks P. Spadea because she convinced and gave me the opportunity to participate in Leg 168, an unforgettable experience. The authors wish to thank the reviewers J. Allan and J. Alt for comments that helped to improve the paper.

## REFERENCES

- Alt, J.C., and Honnorez, J., 1984. Alteration of the upper oceanic crust, DSDP Site 417: mineralogy and chemistry. *Contrib. Mineral. Petrol.*, 87:149–169.
- Alt, J.C., Kinoshita, H., Stokking, L.B., et al., 1993. *Proc. ODP, Init. Repts.*, 148: College Station, TX (Ocean Drilling Program).
- Alt, J.C., Laverne, C., Vanko, D.A., Tartarotti, P., Teagle, D.A.H., Bach, W., Zuleger, E., Erzinger, J., Honnorez, J., Pezard, P.A., Becker, K., Salisbury, M.H., and Wilkens, R.H., 1996. Hydrothermal alteration of a section of upper oceanic crust in the eastern equatorial Pacific: a synthesis of results from Site 504 (DSDP Legs 69, 70, and 83, and ODP Legs 111, 137, 140, and 148.) In Alt, J.C., Kinoshita, H., Stokking, L.B., and Michael, P.J. (Eds.), *Proc. ODP, Sci. Results*, 148: College Station, TX (Ocean Drilling Program), 417–434.
- Andrews, A.J., 1977. Low-temperature fluid alteration of oceanic layer 2 basalts, DSDP Leg 37. *Can. J. Earth Sci.*, 14:911–926.
- , 1980. Saponite and celadonite in Layer 2 basalts, DSDP Leg 37. *Contrib. Mineral. Petrol.*, 73:323–340.
- Baragar, W.R.A., Plant, A.G., Pringle, G.J., and Schau, M., 1977. Petrology and alteration of selected units of Mid-Atlantic Ridge basalts sampled from Sites 332 and 335, DSDP. *Can. J. Earth Sci.*, 14:837–874.
- Böhlke, J.K., Alt, J.C., and Muehlenbachs, K., 1984. Oxygen isotope-water relations in altered deep-sea basalts: low temperature mineralogical controls. *Can. J. Earth Sci.*, 21:67–77.
- Böhlke, J.K., Honnorez, J., and Honnorez-Guerstein, B.M., 1980. Alteration of basalts from site 396B, DSDP: petrographic and mineralogical studies. *Contrib. Mineral. Petrol.*, 73:341–364.
- Böhlke, J.K., Honnorez, J., Honnorez-Guerstein, B.-M., Muehlenbachs, K., and Petersen, N., 1981. Heterogeneous alteration of the upper oceanic crust: correlation of rock chemistry, magnetic properties, and O-isotope ratios with alteration patterns in basalts from Site 396B, DSDP. *J. Geophys. Res.*, 86:7935–7950.
- Buatier, M., Honnorez, J., and Ehret, G., 1989. Fe-smectite-glaucconite transition in hydrothermal clays from Galapagos Spreading Center. *Clays Clay Miner.*, 37:532–541.
- Davis, E.E., Fisher, A.T., Firth, J.V., et al., 1997. *Proc. ODP, Init. Repts.*, 168: College Station, TX (Ocean Drilling Program).
- Davis, E.E., Mottl, M.J., Fisher, A.T., et al., 1992. *Proc. ODP, Init. Repts.*, 139: College Station, TX (Ocean Drilling Program).
- Honnorez, J., Laverne, C., Hubberten, H.-W., Emmermann, R., and Muehlenbachs, K., 1983. Alteration processes in Layer 2 basalts from Deep Sea Drilling Project Hole 504B, Costa Rica Rift. In Cann, J.R., Langseth, M.G., Honnorez, J., Von Herzen, R.P., White, S.M., et al., *Init. Repts. DSDP*, 69: Washington (U.S. Govt. Printing Office), 509–546.
- Hunter, A.G., Kempton, P.D., and Greenwood, P., 1999. Low-temperature fluid-rock interaction: an isotopic and mineralogical perspective of upper crustal evolution, eastern flank of the Juan de Fuca Ridge (JdFR), ODP Leg 168. *Chem. Geol.*, 155:3–28.
- Juteau, T., Bideau, D., Dauteil, O., Manac'h, G., Naidoo, D.D., Nehlig, P., Ondreas, H., Tivey, M.A., Whipple, K.X., and Delaney, J.R., 1995. A submersible study in the western Blanco Fracture Zone, N.E. Pacific: structure and evolution during the last 1.6 Ma. *Mar. Geophys. Res.*, 17:399–430.
- Juteau, T., Noack, Y., Whitechurch, H., and Courtois, C., 1980. Mineralogy and geochemistry of alteration products in Holes 417A and 417D basement samples (Deep Sea Drilling Project Leg 51). In Donnelly, M., Francheteau, J., Bryan, W., Robinson, P., Flower, M., Salisbury, M., et al., *Init. Repts. DSDP*, 51, 52, 53 (Pt. 2): Washington (U.S. Govt. Printing Office), 1273–1279.
- Kastner, M., and Gieskes, J.M., 1976. Interstitial water profiles and sites of diagenetic reactions, Leg 35, DSDP, Bellingshausen Abyssal Plain. *Earth Planet. Sci. Lett.*, 33:11–20.
- Laverne, C., Belarouchi, A., and Honnorez, J., 1996. Alteration mineralogy and chemistry of the upper oceanic crust from Hole 896A, Costa Rica Rift. In Alt, J.C., Kinoshita, H., Stokking, L.B., and Michael, P.J. (Eds.), *Proc. ODP, Sci. Results*, 148: College Station, TX (Ocean Drilling Program), 151–170.
- Li, G., Peacor, D.R., Coombs, D.S., and Kawachi Y., 1997. Solid solution in the celadonite family: the new minerals ferroceldonite,  $K_2Fe_2^{2+}Fe_2^{3+}Si_8O_{20}(OH)_4$ , and ferroaluminoceldonite,  $K_2Fe_2^{2+}Al_2Si_8O_{20}(OH)_4$ . *Am. Mineral.*, 82:503–511.
- McKenzie, W.S., Donaldson, C.H., and Guilford, C., 1982. *Atlas of Igneous Rocks and Their Textures*: New York (Longman Scientific & Technical; Wiley.)
- Natland, J.H., 1980. Crystal morphologies in basalts dredged and drilled from the East Pacific Rise near 9°N and the Siqueiros fracture zone. In Rosendahl, B.R., Hekinian, R., et al., *Init. Repts. DSDP*, 54: Washington (U.S. Govt. Printing Office), 605–634.
- Peacor, D.R., 1992. Diagenesis and low grade metamorphism of shales and slates. *Mineral. Soc. Am. Rev. Mineral.*, 27:335–380.
- Scott, R.B., and Hajash, A., Jr., 1976. Initial submarine alteration of basaltic pillow lavas: a microprobe study. *Am. J. Sci.*, 276:480–501.
- Seyfried, W.E., Jr., Shanks, W.C., III, and Dibble, W.E., Jr., 1978. Clay mineral formation in DSDP Leg 34 basalt. *Earth Planet. Sci. Lett.*, 41:265–276.
- Teagle, D.A.H., Alt, J.C., Bach, W., Halliday, A.N., and Erzinger, J., 1996. Alteration of upper ocean crust in a ridge-flank hydrothermal upflow zone: mineral, chemical, and isotopic constraints from Hole 896A. In Alt, J.C., Kinoshita, H., Stokking, L.B., and Michael, P.J. (Eds.), *Proc. ODP, Sci. Results*, 148: College Station, TX (Ocean Drilling Program), 119–150.
- Wise, W.S., and Eugster, H.P., 1964. Celadonite: synthesis, thermal stability and occurrence. *Am. Mineral.*, 49:1031–1083.

**Date of initial receipt: 4 December 1998**

**Date of acceptance: 4 August 1999**

**Ms 168SR-006**

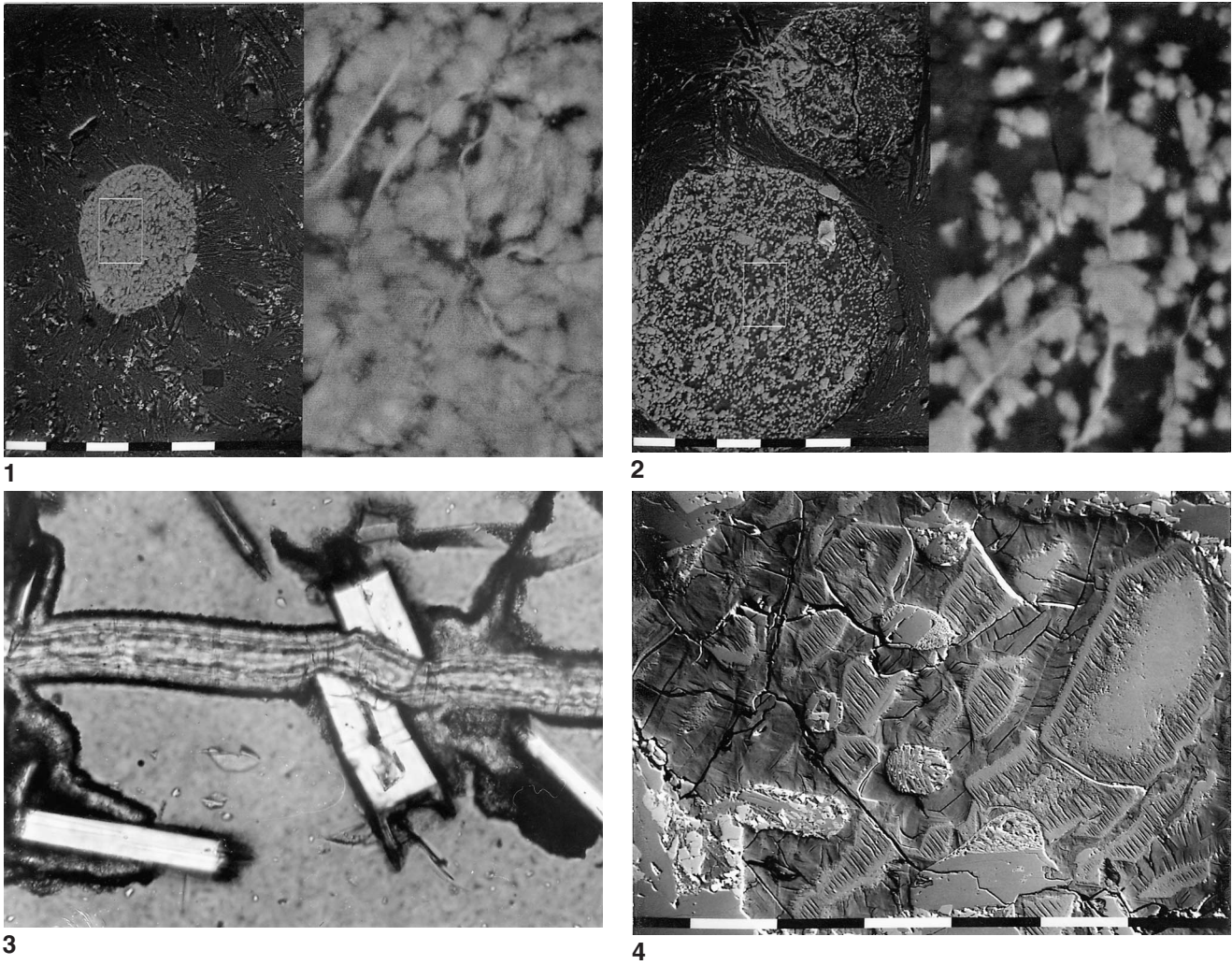


Plate 1. **1.** SEM photomicrograph of vesicle filling within the oxidation halo (enlarged area on the right side). Within vesicle, light gray = iddingsite and dark gray = celadonite; white bar = 50  $\mu\text{m}$ . Sample 168-1026C-17R-1, 13–17 cm (Piece 4). **2.** SEM photomicrograph of vesicles filling within the oxidation halo (enlarged area on the right side). Within vesicles, light gray = iddingsite and dark gray = celadonite; white bar = 50  $\mu\text{m}$ . Sample 168-1026C-17R-1, 13–17 cm (Piece 4). **3.** Photomicrograph of simple vein in glassy margin of Sample 168-1027C-1R-6, 67–70 cm (Piece 2). The layering within the vein is described in the text and sketched in Figure 9A (vein width = 0.5 mm; plane-polarized light). **4.** SEM photomicrograph of pseudomorphic replacement of carbonate (light gray) and Fe-rich saponite (dark gray) after olivine. Saponite fills olivine fractures and is also associated with carbonate in the outer rim of the carbonate clasts. White bar = 100  $\mu\text{m}$ . Sample 168-1027C-5R-5, 22–27 cm (Piece 2).